Scattering matrix method for optical excitation of surface plasmons in metal films with periodic arrays of subwavelength holes

N. Anttu[1] and H. Q. Xu[1,2,*]

[1]*Division of Solid State Physics, Lund University, P.O. Box 118, S-221 00 Lund, Sweden*

[2]*Department of Electronics and Key Laboratory for the Physics and Chemistry of Nanodevices, Peking University, Beijing 100871, China*

(Received 30 November 2010; published 21 April 2011)

We present the formulation of a scattering matrix method for the study of light-scattering properties of metal films. The method is employed for the study of the optical excitation of surface plasmons in a gold film of 15–230 nm thickness, patterned periodically with subwavelength nanoholes. The gold film is placed on a thick SiO_2 wafer, and the nanoholes as well as the top side of the gold film are filled with H_2O. Light is incident on the gold film from either the SiO_2 or the H_2O side. The extinction and reflectance spectra of the system, as well as the electromagnetic field distributions at certain characteristic wavelengths, are calculated. The extinction spectra show, depending on system parameters, one or several peaks in the visible wavelength range. The extinction peaks are found to be caused by surface plasmons. A simple model based on the dispersion relation for surface plasmons in an unperforated gold film is shown to predict the peak positions of the extinction for thick perforated films very well. Even for thin films, this simple model, which includes coupling of surface plasmons on both surfaces of the film, predicts peak positions of the extinction well if the hole diameter is small enough. As the hole diameter increases, the extinction peaks of thin films show redshifts. Extinction peaks caused by surface plasmons at the SiO_2/Au interface in thick films exhibit strong redshifts when the film thickness is decreased. However, the extinction peaks caused by surface plasmons at the H_2O/Au interface in thick films show a completely different behavior. In this case, the extinction peaks do not move noticeably when the film thickness is decreased. Instead, they are weakened and finally disappear. It is also found that each extinction peak is accompanied by an extinction dip and that a reflectance dip is located in the wavelength between the extinction peak and the dip. This arrangement of an extinction peak, a reflectance dip, and an extinction dip is a general property of the surface-plasmon excitation. The calculated electromagnetic field distributions in both thick and thin films show clearly the signature of the excitation of surface plasmons at the extinction peaks, the extinction dips, and the reflectance dips. In thick films with small holes, the electric-field strength in the vicinity of the holes is weak at wavelengths for which surface plasmons are excited. In contrast to this, for thin films at the surface-plasmon excitations, a much stronger electric field is seen in the vicinity of the holes.

DOI: 10.1103/PhysRevB.83.165431 PACS number(s): 78.66.Bz, 78.40.Kc, 78.20.Bh

I. INTRODUCTION

The discovery of the extraordinary optical transmission enhancements through an optically thick metal film patterned with an array of subwavelength holes[1] has initiated great interest in the research society.[2–28] A metal-dielectric interface can support bound surface waves, so called surface plasmons (SP's).[29] SP's cannot be excited by normally incident light in smooth, planar, metal films.[29] Initially, the transmission maxima were found to be closely connected to the excitation of SP's in both hole[1,3,4] and slit[5] arrays, where the periodicity of the array enables the SP excitation. At frequencies corresponding to the transmission maxima, both SP's and hole excitations were seen to occur.[6] These results are in agreement with other studies, which show that both SP's and localized waveguide modes are of importance for the enhanced transmission through a metal film with an array of either holes[7,8] or slits.[9] Furthermore, it has been shown that both the size and geometry of the holes have large impacts on the extraordinary optical transmission.[10–15] Indeed, it is possible to study the extraordinary optical transmission enhancements in terms of coupled modes where the SP's of the continuous film are coupled with the localized waveguide modes of either the nanoholes[16] or the nanoslits.[17]

The transmission spectra of an optically thick metal film perforated with a periodic array of subwavelength holes also exhibit well-defined minima (transmission suppressions). Initially, the transmission suppressions were assumed to be due to the Rayleigh wavelength anomalies.[3,18] The Rayleigh wavelength anomalies occur at frequencies for which one of the diffracted orders is parallel to the film surface.[30] It was, however, noted that both for slits[19] and for two-dimensional (2D) arrays of holes,[6,16,20,24] the positions of the transmission minima seemed to coincide with the frequencies of SP's on unperforated surfaces. In corroboration to this claim, a perturbative approach[21] for SP effects on flat interfaces periodically corrugated by subwavelength apertures has predicted that the transmission suppressions appear at these frequencies. However, the cause of transmission minima in perforated metal films is still claimed from time to time[13–15,22,23] to be due to the Rayleigh wavelength anomalies. A focused investigation on the effect of SP's on the suppressed transmission is, therefore, necessary to clarify the cause of the transmission suppressions.

SP's in nanostructured materials can be used, for example, for beaming and focusing of light transmitted through subwavelength slits,[25–28] for enhancement of the light-emission efficiency of light-emitting diodes,[31] and for decreasing the beam divergence from edge-emitting semiconductor lasers.[32] Biosensing is another field for which nanostructured plasmonic materials are of large interest.[33,34] For all these applications, it is important to know whether SP's in periodic structures cause transmission suppressions.

The objective of this paper is to investigate the impact of SP's on transmission suppressions in both optically thick and thin metal films. We carry out a full electromagnetic field modeling and study the light-propagation properties and electromagnetic field distributions by employing a scattering matrix method. Such a method has been successfully used to study the scattering problems of scalar waves and spinor waves.[35–41] Here, we will employ the formalism to treat the scattering problems of electromagnetic field waves of light, i.e., vector waves, in a dissipative material system. We consider a periodically patterned gold film surrounded by two different homogeneous materials. The periodicity, hole diameter, film thickness, and surrounding materials are varied. We present our results in terms of the (optical) extinction, instead of the transmittance, to emphasize that we move our attention from the extraordinary optical transmission enhancements to the transmission suppressions.

We have found that SP's cause transmission minima (extinction peaks) in both thick and thin, periodically perforated, metal films. We show that an extinction peak in a thick film caused by an SP localized to the interface between the gold film and the homogeneous material of higher refractive index redshifts as the film thickness is decreased. A completely different behavior is found for an extinction peak that is caused in a thick film by an SP localized to the interface between the gold film and the homogeneous material of lower refractive index. In this case, the extinction peak did not move noticeably, but weakened and finally disappeared when the film thickness was decreased. We have also found that each extinction peak is accompanied by an extinction dip and a reflectance dip, and that the reflectance dip is located in the wavelength between the extinction peak and the dip.

The remainder of the paper is organized as follows. We start by introducing the system in Sec. II and presenting a formulation of a general scattering matrix method for light scattering in metal and dielectric films. In Sec. III, we present the results of calculations and discuss the dependencies of the extinction and reflectance spectra on system parameters. We compare the results of the calculated extinction and reflectance spectra with the results obtained for optical excitation of SP's in unperforated films. We also calculate the electromagnetic field distributions at the resonant SP's of the system. Finally, in Sec. IV, we summarize the paper and give concluding remarks.

II. METHOD

A. System

The system we study consists of a gold film of thickness t sandwiched between SiO_2 on the left side and H_2O on the right side, as shown in Fig. 1. Light is incident either from the left or from the right as a plane wave with wave vector $\boldsymbol{k} \cdot \hat{\boldsymbol{e}}_z \neq 0$, where $\hat{\boldsymbol{e}}_z$ is the unit vector along the z axis. There is a periodic array of holes in the gold film. The holes have diameter D and the array has periodicity L in both the x and the y directions. The holes are filled with H_2O. The z axis is chosen in such a way that $z = 0$ and $z = t$ are at the SiO_2/Au and the H_2O/Au interface; see Fig. 1. The x and y axes are chosen so that $x \in [0, L]$ and $y \in [0, L]$ define a unit cell with the center of the hole located at $(L/2, L/2)$; see Fig. 2. The

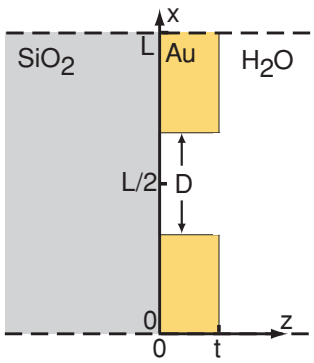

FIG. 1. (Color online) Cross-sectional view of the system studied in this work. The system consists of a gold film of thickness t perforated by a periodic array of subwavelength holes of diameter D and two surrounding materials SiO_2 and H_2O. The holes are filled with H_2O and the array has a period of L in both the x and y directions. Here in the figure only a cross-sectional view of a unit cell of the system is shown.

generalized permittivity $\tilde{\epsilon}$ is material-dependent and can be obtained from

$$\tilde{\epsilon}(\boldsymbol{x}, \omega) = \epsilon_0 n(\boldsymbol{x}, \omega)^2, \tag{1}$$

where ϵ_0 is the permittivity of vacuum and n is the refractive index. In this work, tabulated values of the refractive index n of gold,[42] H_2O,[43] and SiO_2 (Ref. 44) are used for the calculation of $\tilde{\epsilon}$. The system is dissipative but nonmagnetic. The results are presented in terms of the free-space wavelength $\lambda \equiv 2\pi c/\omega$, where c is the speed of light.

B. Scattering matrix method

We present the formulation of a scattering matrix method for the scattering problem of light by a metal material system under the condition that light is incident from a semi-infinite region located either on the left side or on the right side of the system. The method is general in the sense that it allows for the material system to be of arbitrary form and the semi-infinite regions to be of arbitrary homogeneous materials. In addition to the scattered fields (far-field regions), the method can be

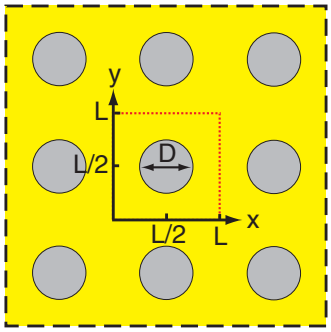

FIG. 2. (Color online) Front view of the gold film in the system with the periodic array of H_2O-filled holes. The holes have a diameter D and the array has a period L in both the x and y directions. Here, only nine unit cells of the system are shown. The dotted line, together with the coordinate system axes, indicates the unit cell used in the simulations.

used to obtain the electromagnetic fields near and inside the material structure in a straightforward manner.

Assume that all the media in the structure have a linear response to the electromagnetic field in the form of

$$\boldsymbol{D}(\boldsymbol{x},\omega) = \tilde{\epsilon}(\boldsymbol{x},\omega)\boldsymbol{E}(\boldsymbol{x},\omega), \tag{2}$$

$$\boldsymbol{B}(\boldsymbol{x},\omega) = \tilde{\mu}(\boldsymbol{x},\omega)\boldsymbol{H}(\boldsymbol{x},\omega), \tag{3}$$

where $\tilde{\mu}(\boldsymbol{x},\omega) \equiv \mu(\boldsymbol{x},\omega)\mu_0$ is the permeability, ω is the frequency of incident light, and $\boldsymbol{E}$, $\boldsymbol{D}$, $\boldsymbol{B}$, and $\boldsymbol{H}$ are the the electric field, the electric displacement, the magnetic induction, and the magnetic field, respectively. Here, we assume $\tilde{\mu}(\boldsymbol{x},\omega) \equiv \mu(\boldsymbol{x},\omega)\mu_0$, where μ_0 is the permeability of vacuum, and hence allow for magnetic materials in the formulation. We also assume that all the time dependencies in $\boldsymbol{E}$, $\boldsymbol{D}$, $\boldsymbol{B}$, and $\boldsymbol{H}$ are of the harmonic form. The Maxwell equations are then written as

$$\begin{aligned}
\nabla \times \boldsymbol{E}(\boldsymbol{x},\omega) &= i\omega\tilde{\mu}(\boldsymbol{x},\omega)\boldsymbol{H}(\boldsymbol{x},\omega),\\
\nabla \times \boldsymbol{H}(\boldsymbol{x},\omega) &= -i\omega\tilde{\epsilon}(\boldsymbol{x},\omega)\boldsymbol{E}(\boldsymbol{x},\omega),\\
\nabla \cdot [\tilde{\mu}(\boldsymbol{x},\omega)\boldsymbol{H}(\boldsymbol{x},\omega)] &= 0,\\
\nabla \cdot [\tilde{\epsilon}(\boldsymbol{x},\omega)\boldsymbol{E}(\boldsymbol{x},\omega)] &= 0.
\end{aligned} \tag{4}$$

To simplify the notations, we will drop the argument ω from all the physical quantities from now on.

To solve Eq. (4) for a given incident light of frequency ω, we divide the system into N slices along the z direction in such a way that both $\tilde{\epsilon}$ and $\tilde{\mu}$ are z-independent in each slice, as schematically shown in Fig. 3. In the schematic figure, z_j is set at the left end of slice j. The semi-infinite regions on the left and the right sides of the structure have z-independent $\tilde{\epsilon}$ and $\tilde{\mu}$ and are denoted as slice 0 and slice $N+1$. The incident light impinges on the system from these semi-infinite regions.

Let us consider the jth slice, in which $z_j \leqslant z \leqslant z_{j+1}$, and denote the z-independent $\tilde{\epsilon}$ and $\tilde{\mu}$ in this slice by $\tilde{\epsilon}_j$ and $\tilde{\mu}_j$. The Maxwell equations, Eq. (4),

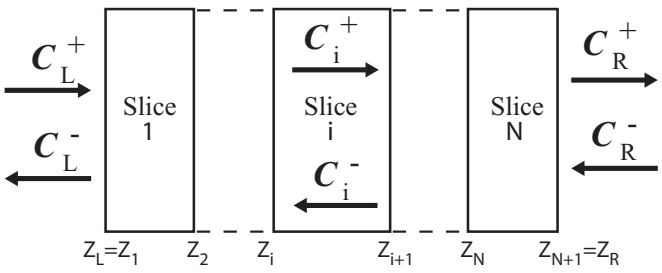

FIG. 3. Schematic view of a system employed in the formulation of the scattering matrix method in this work. The system is divided into N slices in the z direction such that the permittivity and permeability in each slice can be considered to be z-independent. The $\boldsymbol{C}_i^{\pm}$ are expansion coefficients of the field in slice i in terms of the eigenmodes of the slice.

can then be written as[45]

$$\begin{aligned}
\frac{\partial}{\partial z}\begin{bmatrix} E_x^j(\boldsymbol{x}) \\ E_y^j(\boldsymbol{x}) \end{bmatrix} &= \hat{\boldsymbol{T}}_1^j \begin{bmatrix} H_x^j(\boldsymbol{x}) \\ H_y^j(\boldsymbol{x}) \end{bmatrix}\\
&\equiv \begin{bmatrix} \hat{\boldsymbol{T}}_{1,xx}^j & \hat{\boldsymbol{T}}_{1,xy}^j \\ \hat{\boldsymbol{T}}_{1,yx}^j & \hat{\boldsymbol{T}}_{1,yy}^j \end{bmatrix} \begin{bmatrix} H_x^j(\boldsymbol{x}) \\ H_y^j(\boldsymbol{x}) \end{bmatrix},
\end{aligned} \tag{5}$$

$$\begin{aligned}
\frac{\partial}{\partial z}\begin{bmatrix} H_x^j(\boldsymbol{x}) \\ H_y^j(\boldsymbol{x}) \end{bmatrix} &= \hat{\boldsymbol{T}}_2^j \begin{bmatrix} E_x^j(\boldsymbol{x}) \\ E_y^j(\boldsymbol{x}) \end{bmatrix}\\
&\equiv \begin{bmatrix} \hat{\boldsymbol{T}}_{2,xx}^j & \hat{\boldsymbol{T}}_{2,xy}^j \\ \hat{\boldsymbol{T}}_{2,yx}^j & \hat{\boldsymbol{T}}_{2,yy}^j \end{bmatrix} \begin{bmatrix} E_x^j(\boldsymbol{x}) \\ E_y^j(\boldsymbol{x}) \end{bmatrix},
\end{aligned} \tag{6}$$

where E_x^j and E_y^j (H_x^j and H_y^j) are the x and y components of the electric field $\boldsymbol{E}^j$ (the magnetic field $\boldsymbol{H}^j$) in the jth slice and the operators $\hat{\boldsymbol{T}}_1^j$ and $\hat{\boldsymbol{T}}_2^j$ are given by

$$\begin{aligned}
\hat{\boldsymbol{T}}_{1,xx}^j &= \frac{1}{i\omega}\frac{\partial}{\partial x}\frac{1}{\tilde{\epsilon}_j(x,y)}\frac{\partial}{\partial y},\\
\hat{\boldsymbol{T}}_{1,xy}^j &= i\omega\tilde{\mu}_j(x,y) - \frac{1}{i\omega}\frac{\partial}{\partial x}\frac{1}{\tilde{\epsilon}_j(x,y)}\frac{\partial}{\partial x},\\
\hat{\boldsymbol{T}}_{1,yx}^j &= -i\omega\tilde{\mu}_j(x,y) + \frac{1}{i\omega}\frac{\partial}{\partial y}\frac{1}{\tilde{\epsilon}_j(x,y)}\frac{\partial}{\partial y},\\
\hat{\boldsymbol{T}}_{1,yy}^j &= -\frac{1}{i\omega}\frac{\partial}{\partial y}\frac{1}{\tilde{\epsilon}_j(x,y)}\frac{\partial}{\partial x},
\end{aligned} \tag{7}$$

and

$$\begin{aligned}
\hat{\boldsymbol{T}}_{2,xx}^j &= -\frac{1}{i\omega}\frac{\partial}{\partial x}\frac{1}{\tilde{\mu}_j(x,y)}\frac{\partial}{\partial y},\\
\hat{\boldsymbol{T}}_{2,xy}^j &= -i\omega\tilde{\epsilon}_j(x,y) + \frac{1}{i\omega}\frac{\partial}{\partial x}\frac{1}{\tilde{\mu}_j(x,y)}\frac{\partial}{\partial x},\\
\hat{\boldsymbol{T}}_{2,yx}^j &= i\omega\tilde{\epsilon}_j(x,y) - \frac{1}{i\omega}\frac{\partial}{\partial y}\frac{1}{\tilde{\mu}_j(x,y)}\frac{\partial}{\partial y},\\
\hat{\boldsymbol{T}}_{2,yy}^j &= \frac{1}{i\omega}\frac{\partial}{\partial y}\frac{1}{\tilde{\mu}_j(x,y)}\frac{\partial}{\partial x}.
\end{aligned} \tag{8}$$

Combining Eqs. (5) and (6) gives

$$\frac{\partial^2}{\partial z^2}\begin{bmatrix} E_x^j(\boldsymbol{x}) \\ E_y^j(\boldsymbol{x}) \end{bmatrix} = \hat{\boldsymbol{T}}_1^j\hat{\boldsymbol{T}}_2^j \begin{bmatrix} E_x^j(\boldsymbol{x}) \\ E_y^j(\boldsymbol{x}) \end{bmatrix}. \tag{9}$$

This equation has, as possible solutions, eigenmodes of the form $\tilde{\boldsymbol{E}}_j^{\alpha}(\boldsymbol{x}) = \tilde{\boldsymbol{E}}_j^{\alpha}(x,y)e^{\pm ik_j^{\alpha}(z-z_j)}$, where $\tilde{\boldsymbol{E}}_j^{\alpha}(x,y) = [\tilde{E}_{j,x}^{\alpha}(x,y), \tilde{E}_{j,y}^{\alpha}(x,y)]^T$. By employing a complete, orthonormal basis, $\{\phi_m(x,y)\}$, the eigenmodes can be obtained from the matrix eigenvalue equation,

$$\beta_j^{\alpha}\boldsymbol{d}_j^{\alpha} = -\boldsymbol{T}_1^j\boldsymbol{T}_2^j\boldsymbol{d}_j^{\alpha}, \tag{10}$$

where $\beta_j^{\alpha} = (k_j^{\alpha})^2$, $\boldsymbol{T}_{\lambda}^j$ is the operator matrix obtained when the operator $\hat{\boldsymbol{T}}_{\lambda}^j$ is projected onto the basis $\{\phi_m(x,y)\}$, i.e., $\boldsymbol{T}_{\lambda}^j$ is a 2×2 block matrix whose elements in block $\ell\ell'$ are given by $(\boldsymbol{T}_{\lambda,\ell\ell'}^j)_{mn} = \langle\phi_m|\hat{\boldsymbol{T}}_{\lambda,\ell\ell'}^j|\phi_n\rangle$, and $\boldsymbol{d}_j^{\alpha}$ contains the expansion

coefficients of $\tilde{\boldsymbol{E}}_j^{\alpha}(x,y)$ in the basis $\{\phi_m(x,y)\}$ and can be written in the vector form of

$$\boldsymbol{d}_j^{\alpha} = \begin{bmatrix} \boldsymbol{d}_{j,x}^{\alpha} \\ \boldsymbol{d}_{j,y}^{\alpha} \end{bmatrix}. \tag{11}$$

A general solution for the electric field, $\boldsymbol{E}^j(\boldsymbol{x}) = [E_x^j(\boldsymbol{x}), E_y^j(\boldsymbol{x})]^T$, in slice j can be expressed in terms of the eigenmodes as[46]

$$\begin{aligned} E_{x(y)}^j(\boldsymbol{x}) &= \sum_{\alpha} \tilde{E}_{j,x(y)}^{\alpha}(x,y)\left[C_j^{+,\alpha} e^{ik_j^{\alpha}(z-z_j)} + C_j^{-,\alpha} e^{-ik_j^{\alpha}(z-z_j)}\right] \\ &= \sum_{\alpha}\sum_{m} d_{j,x(y),m}^{\alpha}\phi_m(x,y) \\ &\quad \times \left[C_j^{+,\alpha} e^{ik_j^{\alpha}(z-z_j)} + C_j^{-,\alpha} e^{-ik_j^{\alpha}(z-z_j)}\right]. \end{aligned} \tag{12}$$

In the above equation, the complex-valued wave vectors k_j^{α} are obtained from

$$k_j^{\alpha} = \sqrt{\beta_j^{\alpha}}, \tag{13}$$

under the rule that $\mathrm{Re}\, k_j^{\alpha} > 0$ if $\mathrm{Im}\, k_j^{\alpha} = 0$ and $\mathrm{Im}\, k_j^{\alpha} > 0$ if $\mathrm{Im} k_j^{\alpha} \neq 0$. Thus, $\{C_j^{+,\alpha}\}$ are the expansion coefficients in terms of those eigenmodes α, which are either propagating forward or exponentially decaying along the positive z direction and $\{C_j^{-,\alpha}\}$ are the expansion coefficients in terms of those eigenmodes α which are either propagating backward or exponentially growing along the z direction. Similarly, the magnetic field $\boldsymbol{H}^j(\boldsymbol{x}) = [H_x^j(\boldsymbol{x}), H_y^j(\boldsymbol{x})]^T$ in slice j can be expressed as

$$\begin{aligned} H_{x(y)}^j(\boldsymbol{x}) &= \sum_{\alpha}\sum_{m} h_{j,x(y),m}^{\alpha}\phi_m(x,y) \\ &\quad \times \left[C_j^{+,\alpha} e^{ik_j^{\alpha}(z-z_j)} - C_j^{-,\alpha} e^{-ik_j^{\alpha}(z-z_j)}\right], \end{aligned} \tag{14}$$

where the expansion coefficients $\{h_{j,x}^{\alpha}\}$ and $\{h_{j,y}^{\alpha}\}$ can be derived, with the use of Eq. (5), as

$$\boldsymbol{h}_j^{\alpha} = \begin{bmatrix} \boldsymbol{h}_{j,x}^{\alpha} \\ \boldsymbol{h}_{j,y}^{\alpha} \end{bmatrix} = ik_j^{\alpha}\left(\boldsymbol{T}_1^j\right)^{-1}\boldsymbol{d}_j^{\alpha}. \tag{15}$$

Obviously, we have a set of unknown coefficients $\{C_j^{+,\alpha}\}$ and $\{C_j^{-,\alpha}\}$ in the expansions of the electric and magnetic fields, $\boldsymbol{E}^j(\boldsymbol{x})$ and $\boldsymbol{H}^j(\boldsymbol{x})$, in each slice region. However, from the Maxwell equations, it can be shown that at the interface between two adjacent slices, the transverse components of the electric and magnetic fields are continuous. Thus, a matrix equation that connects the expansion coefficients $\{C_j^{+,\alpha}\}$ and $\{C_j^{-,\alpha}\}$ in slice j with the expansion coefficients $\{C_{j+1}^{+,\alpha}\}$ and $\{C_{j+1}^{-,\alpha}\}$ in slice $j+1$ can be derived,

$$\begin{bmatrix} \boldsymbol{P}_{j+1} & \boldsymbol{P}_{j+1} \\ \boldsymbol{Q}_{j+1} & -\boldsymbol{Q}_{j+1} \end{bmatrix}\begin{bmatrix} \boldsymbol{C}_{j+1}^{+} \\ \boldsymbol{C}_{j+1}^{-} \end{bmatrix} = \begin{bmatrix} \boldsymbol{P}_j & \boldsymbol{P}_j \\ \boldsymbol{Q}_j & -\boldsymbol{Q}_j \end{bmatrix}\begin{bmatrix} \boldsymbol{\gamma}_j & \boldsymbol{0} \\ \boldsymbol{0} & \boldsymbol{\gamma}_j^{-1} \end{bmatrix}\begin{bmatrix} \boldsymbol{C}_j^{+} \\ \boldsymbol{C}_j^{-} \end{bmatrix}, \tag{16}$$

where

$$(\boldsymbol{P}_j)_{n\alpha} = \left(\boldsymbol{d}_j^{\alpha}\right)_n, \tag{17}$$

$$(\boldsymbol{Q}_j)_{n\alpha} = \left(\boldsymbol{h}_j^{\alpha}\right)_n, \tag{18}$$

$$(\boldsymbol{\gamma}_j)_{m\alpha} = \delta_{m,\alpha} e^{ik_j^{\alpha}(z_{j+1}-z_j)}. \tag{19}$$

Equation (16) can be rewritten, to define the transfer matrix $\boldsymbol{M}(j,j+1)$, as

$$\begin{bmatrix} \boldsymbol{C}_j^{+} \\ \boldsymbol{C}_j^{-} \end{bmatrix} = \begin{bmatrix} \boldsymbol{M}_{11}(j,j+1) & \boldsymbol{M}_{12}(j,j+1) \\ \boldsymbol{M}_{21}(j,j+1) & \boldsymbol{M}_{22}(j,j+1) \end{bmatrix}\begin{bmatrix} \boldsymbol{C}_{j+1}^{+} \\ \boldsymbol{C}_{j+1}^{-} \end{bmatrix}, \tag{20}$$

where the submatrices of $\boldsymbol{M}(j,j+1)$ are defined by

$$\begin{aligned} \boldsymbol{M}_{11}(j,j+1) &= \boldsymbol{\gamma}_j^{-1}\boldsymbol{\mathcal{T}}_{11}(j,j+1), \\ \boldsymbol{M}_{12}(j,j+1) &= \boldsymbol{\gamma}_j^{-1}\boldsymbol{\mathcal{T}}_{12}(j,j+1), \\ \boldsymbol{M}_{21}(j,j+1) &= \boldsymbol{\gamma}_j\boldsymbol{\mathcal{T}}_{12}(j,j+1), \\ \boldsymbol{M}_{22}(j,j+1) &= \boldsymbol{\gamma}_j\boldsymbol{\mathcal{T}}_{11}(j,j+1), \end{aligned} \tag{21}$$

with

$$\begin{aligned} \boldsymbol{\mathcal{T}}_{11}(j,j+1) &= \tfrac{1}{2}\left(\boldsymbol{P}_j^{-1}\boldsymbol{P}_{j+1} + \boldsymbol{Q}_j^{-1}\boldsymbol{Q}_{j+1}\right), \\ \boldsymbol{\mathcal{T}}_{12}(j,j+1) &= \tfrac{1}{2}\left(\boldsymbol{P}_j^{-1}\boldsymbol{P}_{j+1} - \boldsymbol{Q}_j^{-1}\boldsymbol{Q}_{j+1}\right). \end{aligned} \tag{22}$$

It is possible in principle to calculate the total transfer matrix for the whole system, which connects the expansion coefficients of the electric and magnetic fields, $\{C_R^{+,\alpha}\}$ and $\{C_R^{-,\alpha}\}$, in the right semi-infinite homogeneous region to the expansion coefficients of the electric and magnetic fields, $\{C_L^{+,\alpha}\}$ and $\{C_L^{-,\alpha}\}$, in the left semi-infinite homogeneous region, by successive multiplications of individual transfer matrices, $\{\boldsymbol{M}(j,j+1)\}$. It is, however, known that in the calculation for the total transfer matrix, one often suffers from a numerical instability due to the presence of both the exponentially growing and exponentially decaying terms in the formulation (see Ref. 35 for details). This numerical instability can be removed from the calculations by reformulating the problem with the use of a scattering matrix method.[35,36,38,39] The essence of the method is to convert all the exponentially growing terms to exponentially decaying terms and let propagating modes rather than evanescent modes dominate in the numerical calculations. This can be realized by coupling explicitly the outgoing electromagnetic waves, $\{C_R^{+,\alpha}\}$ and $\{C_L^{-,\alpha}\}$, to the incoming electromagnetic waves, $\{C_L^{+,\alpha}\}$ and $\{C_R^{-,\alpha}\}$, via the equation[35]

$$\begin{bmatrix} \boldsymbol{C}_R^{+} \\ \boldsymbol{C}_L^{-} \end{bmatrix} = \boldsymbol{S}(L,R)\begin{bmatrix} \boldsymbol{C}_L^{+} \\ \boldsymbol{C}_R^{-} \end{bmatrix} = \begin{bmatrix} \boldsymbol{S}_{11}(L,R) & \boldsymbol{S}_{12}(L,R) \\ \boldsymbol{S}_{21}(L,R) & \boldsymbol{S}_{22}(L,R) \end{bmatrix}\begin{bmatrix} \boldsymbol{C}_L^{+} \\ \boldsymbol{C}_R^{-} \end{bmatrix}, \tag{23}$$

where $\boldsymbol{S}(L,R)$ is the scattering matrix for the total system and can be obtained by an iterative procedure as described in Ref. 35.

Let $\boldsymbol{S}(L,j)$ denote the scattering matrix for the subsystem consisting of the first j slices and the left semi-infinite homogeneous region, i.e.,

$$\begin{bmatrix} \boldsymbol{C}_j^{+} \\ \boldsymbol{C}_L^{-} \end{bmatrix} = \begin{bmatrix} \boldsymbol{S}_{11}(L,j) & \boldsymbol{S}_{12}(L,j) \\ \boldsymbol{S}_{21}(L,j) & \boldsymbol{S}_{22}(L,j) \end{bmatrix}\begin{bmatrix} \boldsymbol{C}_L^{+} \\ \boldsymbol{C}_j^{-} \end{bmatrix}. \tag{24}$$

With the help of the transfer matrix defined in Eq. (20), an iterative relation for the scattering matrix $\boldsymbol{S}(L,j+1)$ can be derived,[35]

$$\begin{aligned} \boldsymbol{S}_{11}(L,j+1) &= \left[\boldsymbol{1} - \boldsymbol{M}_{11}^{-1}(j,j+1)\boldsymbol{S}_{12}(L,j)\right. \\ &\quad \left.\times \boldsymbol{M}_{21}(j,j+1)\right]^{-1} \\ &\quad \times \boldsymbol{M}_{11}^{-1}(j,j+1)\boldsymbol{S}_{11}(L,j), \end{aligned}$$

$$\begin{aligned}
\boldsymbol{S}_{12}(L,j+1) &= \big[\mathbf{1} - \boldsymbol{M}_{11}^{-1}(j,j+1)\boldsymbol{S}_{12}(L,j) \\
&\quad \times \boldsymbol{M}_{21}(j,j+1)\big]^{-1}\big[\boldsymbol{M}_{11}^{-1}(j,j+1) \\
&\quad \boldsymbol{S}_{12}(L,j)\boldsymbol{M}_{22}(j,j+1) \\
&\quad - \boldsymbol{M}_{11}^{-1}(j,j+1)\boldsymbol{M}_{12}(j,j+1)\big], \\
\boldsymbol{S}_{21}(L,j+1) &= \boldsymbol{S}_{22}(L,j)\boldsymbol{M}_{21}(j,j+1)\boldsymbol{S}_{11}(L,j+1) \\
&\quad + \boldsymbol{S}_{21}(L,j), \\
\boldsymbol{S}_{22}(L,j+1) &= \boldsymbol{S}_{22}(L,j)\boldsymbol{M}_{21}(j,j+1)\boldsymbol{S}_{12}(L,j+1) \\
&\quad + \boldsymbol{S}_{22}(L,j)\boldsymbol{M}_{22}(j,j+1). \qquad (25)
\end{aligned}$$

In the above equations, the exponentially growing factors of the form $\boldsymbol{\gamma}_i^{-1}$, which can cause numerical instability as discussed above, do not appear. This is seen by inserting $\boldsymbol{M}_{\ell\ell'}$ defined in Eq. (21) into Eq. (25) and employing matrix equations $[\boldsymbol{\mathcal{T}}_{\ell\ell'}\boldsymbol{\gamma}_j]^{-1} = \boldsymbol{\gamma}_j^{-1}\boldsymbol{\mathcal{T}}_{\ell\ell'}^{-1}$ and $\boldsymbol{\gamma}_j\boldsymbol{\gamma}_j^{-1} = \mathbf{1}$. Here, the reduction of $\boldsymbol{\gamma}_j\boldsymbol{\gamma}_j^{-1}$ to $\mathbf{1}$ in Eq. (25) must, of course, be done analytically and not numerically.

The iteration is started by setting $\boldsymbol{S}(L,0) \equiv \mathbf{1}$ and continued until $\boldsymbol{S}(L,R) \equiv \boldsymbol{S}(L,N+1)$ is obtained. With the help of the transfer matrices defined in Eqs. (20) and (21), the scattering matrix $\boldsymbol{S}(j,R)$ for a subsystem consisting of slices j to N and the right semi-infinite homogeneous region can also be obtained from the iteration equations given in Eq. (25) by setting $L = j$ and $\boldsymbol{S}(j,j) \equiv \mathbf{1}$.

Once the scattering matrices $\boldsymbol{S}(L,j)$ and $\boldsymbol{S}(j,R)$ are obtained, the expansion coefficients appearing in Eqs. (12) and (14) for the transverse components of the electric and magnetic fields in the jth slice can be calculated from[47]

$$\begin{aligned}
\boldsymbol{C}_j^+ &= \big[1 - \boldsymbol{S}_{12}(L,j)\boldsymbol{S}_{21}(j,R)\big]^{-1} \\
&\quad \times\big[\boldsymbol{S}_{11}(L,j)\boldsymbol{C}_L^+ + \boldsymbol{S}_{12}(L,j)\boldsymbol{S}_{22}(j,R)\boldsymbol{C}_R^-\big], \qquad (26) \\
\boldsymbol{C}_j^- &= \big[1 - \boldsymbol{S}_{21}(j,R)\boldsymbol{S}_{12}(L,j)\big]^{-1} \\
&\quad \times\big[\boldsymbol{S}_{21}(j,R)\boldsymbol{S}_{11}(L,j)\boldsymbol{C}_L^+ + \boldsymbol{S}_{22}(j,R)\boldsymbol{C}_R^-\big]. \qquad (27)
\end{aligned}$$

The corresponding z components of the fields are obtained from

$$H_z^j = \frac{1}{i\omega\tilde{\mu}_j}\left[\frac{\partial E_y^j}{\partial x} - \frac{\partial E_x^j}{\partial y}\right], \qquad (28)$$

$$E_z^j = \frac{1}{i\omega\tilde{\epsilon}_j}\left[\frac{\partial H_x^j}{\partial y} - \frac{\partial H_y^j}{\partial x}\right]. \qquad (29)$$

C. Boundary conditions and energy flow

It is seen from Eqs. (23), (26), and (27) that the electromagnetic waves can be uniquely determined from the expansion coefficient vectors, $\boldsymbol{C}_L^+$ and $\boldsymbol{C}_R^-$, of given incident lights in the left and right homogeneous regions of the system. By orthogonalizing all the eigenmodes in the homogeneous left and right regions according to

$$\boldsymbol{d}_{L(R)}^{\alpha} \cdot \boldsymbol{d}_{L(R)}^{\beta,*} = \delta_{\alpha,\beta}, \qquad (30)$$

the expansion coefficient vectors, $\boldsymbol{C}_L^+$ and $\boldsymbol{C}_R^-$, can be obtained from

$$\begin{aligned}
C_L^{+,\alpha} &= \int \big[E_x^L(x,y,z)\tilde{E}_{L,x}^{\alpha,*}(x,y) \\
&\quad + E_y^L(x,y,z)\tilde{E}_{L,y}^{\alpha,*}(x,y)\big]e^{-ik_L^{\alpha}(z-z_L)}dx\,dy, \qquad (31)
\end{aligned}$$

and

$$\begin{aligned}
C_R^{-,\alpha} &= \int \big[E_x^R(x,y,z)\tilde{E}_{R,x}^{\alpha,*}(x,y) \\
&\quad + E_y^R(x,y,z)\tilde{E}_{R,y}^{\alpha,*}(x,y)\big]e^{ik_R^{\alpha}(z-z_R)}dx\,dy, \qquad (32)
\end{aligned}$$

where $E_x^L(x,y,z)$ and $E_y^L(x,y,z)$ with $(z < z_L)$ are the x and y components of the electric field of the incident light from the left, and $E_x^R(x,y,z)$ and $E_y^R(x,y,z)$ with $(z > z_R)$ are the x and y components of the electric field of the incident light from the right. In a light-scattering experiment, light is often sent in from one side. In this case, the boundary condition of the light-scattering problem is specified by the expansion coefficient vector of the incident light on the injection side and by setting the expansion coefficient vector of the incident light on the other side to zero. For example, when one considers the case in which light is incident from the left, only the expansion coefficient vector $\boldsymbol{C}_L^+$ needs to be calculated as above, and the other expansion coefficient vector $\boldsymbol{C}_R^-$ can be simply set to $\boldsymbol{C}_R^- = \mathbf{0}$.

For the energy flow calculation, it is convenient to classify all the eigenmodes in the left and right homogeneous regions to the groups of transverse electric (TE), transverse magnetic (TM), and transverse electromagnetic (TEM) modes. Here, by a TE mode we mean a mode for which $\tilde{E}_{L(R),z}^{\alpha}(x,y) = 0$ for all x and y but $\tilde{H}_{L(R),z}^{\alpha}(x,y) \neq 0$ may hold in general. By a TM mode we mean a mode for which $\tilde{H}_{L(R),z}^{\alpha}(x,y) = 0$ for all x and y but $\tilde{E}_{L(R),z}^{\alpha}(x,y) \neq 0$ may hold in general. Finally, by a TEM mode we mean a mode for which both $\tilde{E}_{L(R),z}^{\alpha}(x,y) = 0$ and $\tilde{H}_{L(R),z}^{\alpha}(x,y) = 0$ for all x and y. We use this definition, where a TEM mode is not considered as a TE or TM mode, to avoid double counting in the following. The z components of a given mode can be calculated from the x and y components of the mode by Eqs. (28) and (29).

The time-averaged flux of energy is given by the real Poynting vector

$$\boldsymbol{S}(\boldsymbol{x}) = \tfrac{1}{4}[\boldsymbol{E}(\boldsymbol{x}) \times \boldsymbol{H}^*(\boldsymbol{x}) + \boldsymbol{E}^*(\boldsymbol{x}) \times \boldsymbol{H}(\boldsymbol{x})]. \qquad (33)$$

In the left and right homogeneous regions, the energy flow in the positive z direction through the x-y plane can be derived, using the normalization condition of Eq. (30), as

$$\begin{aligned}
I_{L(R)} &= \int S_z(x,y,z)dx\,dy \\
&= \sum_{\alpha}^{\{\mathrm{Re}\}} \gamma_{L(R),M_{\alpha}^{L(R)}}^{\alpha}\left[\left|C_{L(R)}^{+,\alpha}\right|^2 - \left|C_{L(R)}^{-,\alpha}\right|^2\right], \qquad (34)
\end{aligned}$$

where {Re} denotes summation over only those α for which $k_{L(R)}^{\alpha}$ is a real number, $M_{\alpha}^{L(R)}$=TE, TM, or TEM denotes the type of the αth mode, and

$$\gamma_{L(R),\mathrm{TE}}^{\alpha} = \frac{k_{L(R)}^{\alpha}}{2\omega\tilde{\mu}_{L(R)}}, \qquad (35)$$

$$\gamma_{L(R),\mathrm{TM}}^{\alpha} = \frac{\omega\tilde{\epsilon}_{L(R)}}{2k_{L(R)}^{\alpha}}, \qquad (36)$$

$$\gamma_{L(R),\mathrm{TEM}}^{\alpha} = \frac{k_{L(R)}^{\alpha}}{2\omega\tilde{\mu}_{L(R)}}. \qquad (37)$$

In deriving Eq. (34), we have employed the assumption that the media in the left and right homogeneous regions are lossless dielectric materials, i.e., $\tilde{\epsilon}_{L(R)}$ and $\tilde{\mu}_{L(R)}$ are real, positive

values, and thus $k^{\alpha}_{L(R)}$ is either a real or a purely imaginary number.

As seen from Eq. (34), the energy flows in the left and right homogeneous regions are, as expected, independent of coordinate z. Furthermore, the flows in the forward and backward directions can be distinguished and an expression for the energy flow carried by each mode can be obtained. It is now possible to define the transmittance and the reflectance for the case in which light is incident onto the system from one side only. By taking the case in which light is incident from the left, the incident, transmitted, and reflected energy flows are, as seen from Eq. (34), given by

$$I_I = \sum_{\alpha}^{\{\mathrm{Re}\}} \gamma^{\alpha}_{L,M^L_{\alpha}} \left|C^{+,\alpha}_L\right|^2, \tag{38}$$

$$I_T = \sum_{\alpha}^{\{\mathrm{Re}\}} \gamma^{\alpha}_{R,M^R_{\alpha}} \left|C^{+,\alpha}_R\right|^2, \tag{39}$$

$$I_R = \sum_{\alpha}^{\{\mathrm{Re}\}} \gamma^{\alpha}_{L,M^L_{\alpha}} \left|C^{-,\alpha}_L\right|^2. \tag{40}$$

The total transmittance and reflectance can be found from

$$T \equiv I_T/I_I, \tag{41}$$

$$R \equiv I_R/I_I, \tag{42}$$

while the transmittance and reflectance into the αth eigenmode are given by

$$T_{\alpha} \equiv I_{T,\alpha}/I_I, \tag{43}$$

$$R_{\alpha} \equiv I_{R,\alpha}/I_I, \tag{44}$$

where

$$I_{T,\alpha} \equiv \gamma^{\alpha}_{R,M^R_{\alpha}} \left|C^{+,\alpha}_R\right|^2, \tag{45}$$

$$I_{R,\alpha} \equiv \gamma^{\alpha}_{L,M^L_{\alpha}} \left|C^{-,\alpha}_L\right|^2. \tag{46}$$

D. Periodic system

We now apply the method formulated above to a two-dimensional periodic scattering system with periods of L_x and L_y in the x and y directions, respectively. The incident light is assumed to be a plane wave incident from a direction given by $\boldsymbol{k} = (k_x, k_y, k_z)$. An appropriate basis for solving for eigenmodes [Eq. (10)] for this periodic system can be chosen, according to Bloch's theorem, as $\{\phi_m(x,y)\}$ with $\phi_m(x,y)$ given by

$$\phi_m(x,y) = \frac{1}{\sqrt{L_x}} e^{ik_{x,n_x}x} \frac{1}{\sqrt{L_y}} e^{ik_{y,n_y}y}, \tag{47}$$

where n_x and n_y are integers and

$$k_{x,n_x} = \frac{2\pi}{L_x} n_x + k_x, \tag{48}$$

$$k_{y,n_y} = \frac{2\pi}{L_y} n_y + k_y. \tag{49}$$

From the Maxwell equations, Eq. (4), it can be shown that the plane waves given in Eq. (47) are eigensolutions to the left and right homogeneous regions. Thus, associated with each basis function $\phi_m(x,y)$, one can find, in general, one TE and one TM eigenmode with wave vector

$$k^2_{z,L(R)} = \tilde{\epsilon}_{L(R)}\tilde{\mu}_{L(R)}\omega^2 - k^2_{x,n_x} - k^2_{y,n_y}. \tag{50}$$

However, in the case of $k_{x,n_x} = k_{y,n_y} = 0$, the two corresponding eigenmodes of the electromagnetic wave are in fact TEM modes. We call the modes having $n_x = n_y = 0$ the zeroth-order diffracted modes, and all other modes are higher-order diffracted modes. We further define the zeroth-order transmittance T_{00} for a periodic scattering system under illumination by a TEM plane wave as the sum of transmittances into the two zeroth-order diffracted modes, i.e.,

$$T_{00} \equiv T_a + T_b, \tag{51}$$

where a and b denote the two TEM modes having $n_x = n_y = 0$. We define similarly the zeroth-order reflectance R_{00} as the sum of reflectances into the two zeroth-order diffracted modes, i.e.,

$$R_{00} \equiv R_a + R_b. \tag{52}$$

We note that in numerical calculations, the ranges of n_x and n_y must be limited. We limit them by setting

$$-N_x \leqslant n_x \leqslant N_x, \tag{53}$$

$$-N_y \leqslant n_y \leqslant N_y, \tag{54}$$

where N_x and N_y are two large integer numbers, so that $\boldsymbol{T}^j_1$ and $\boldsymbol{T}^j_2$ in Eq. (10) are two $2(2N_x+1)(2N_y+1) \times 2(2N_x+1)(2N_y+1)$ matrices. In the calculations, we have let N_x and N_y be large enough so that a required numerical accuracy is achieved. The numerical convergence rate can be enhanced with use of the fast Fourier factorization method[48] (see Appendix B for details). We also note that incident light of arbitrary form can be decomposed into plane waves. The scattering problem for each plane-wave component can be solved for separately, and the total solution can be obtained from a linear combination of the solutions for all the plane-wave components.

III. RESULTS

We study the optical response of the nonmagnetic ($\tilde{\mu} = \mu_0$) system described in detail in Sec. II A. The system consists of a perforated gold film surrounded by SiO_2 on the left side and H_2O on the right side, as shown in Figs. 1 and 2. We consider the situation in which an x-polarized plane wave is incident normally, with $k_x = k_y = 0$, toward the film either from the left or from the right. Thus, we set $\boldsymbol{E}^L(x,y,z_L) = \hat{\boldsymbol{e}}_x$ and $\boldsymbol{E}^R(x,y,z_R) = \boldsymbol{0}$ in Eqs. (31) and (32) when light is incident from the left and $\boldsymbol{E}^L(x,y,z_L) = \boldsymbol{0}$ and $\boldsymbol{E}^R(x,y,z_R) = \hat{\boldsymbol{e}}_x$ when light is incident from the right.

In the simulations, we find that the zeroth-order transmittance T_{00}, defined in Eq. (51), does not depend on the side from which light is incident. This invariance of T_{00} is in agreement with the experiments on periodically perforated silver films reported in Ref. 3 and the analytical proof for linear and locally responding media shown in Ref. 49. Transmission properties

of the system are often presented in terms of the (optical) extinction

$$\eta \equiv \log_{10}\left(\frac{1}{T_{00}}\right), \tag{55}$$

which is, again, independent of the side from which light is incident. In general, the resonances we are interested in are present both in the extinction and the total transmittance spectra. However, in many cases, the resonances occurred at long wavelengths for which all the higher-order diffracted modes are of evanescent type and only the zeroth-order diffracted modes are of propagating type. At those wavelengths, $T_{00} = T$ and thus η gives the information of T.

A. Excitation spectra

We begin with the study of the extinction spectra of perforated gold film systems. Figure 4 shows the extinction spectra of the perforated gold film system with periodicities of $L_x = L_y = L = 333$ nm and hole diameter of $D = 140$ nm for different values of the film thickness t. An anomaly in the form of an extinction peak is clearly present in each curve and shows redshift when the film thickness is decreased. The extinction peak is at $\lambda \approx 570$ nm for $t = 230$ nm and is redshifted by almost 250 nm when t is decreased to 15 nm. This t dependence contradicts the common[3,13–15,18,22,23] assumption that it is the Rayleigh wavelength anomaly that causes transmission minima (extinction peaks) in periodically perforated metal films. A Rayleigh wavelength anomaly can occur when one of the TE or TM eigenmodes in the superstrate or substrate is parallel to the surface,[30] i.e., when $k_{z,L} = 0$ or $k_{z,R} = 0$ in Eq. (50) for some n_x and n_y. This condition is independent of t. Thus, the Rayleigh wavelength anomaly cannot explain the t dependence of the position of the extinction peak shown in Fig. 4.

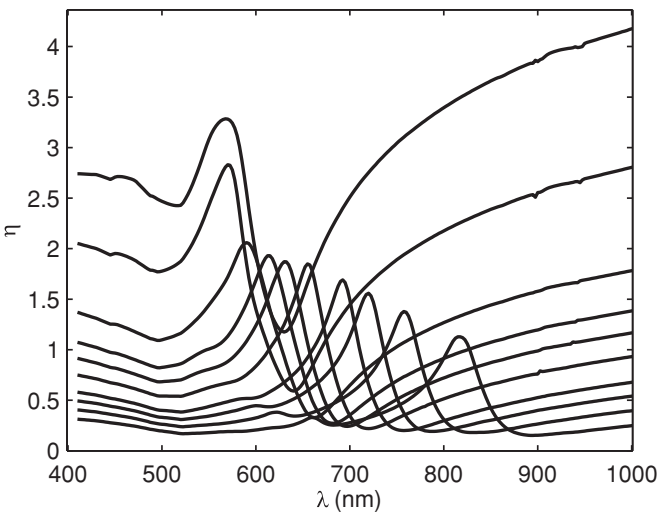

FIG. 4. Calculated extinction spectra for the system shown in Figs. 1 and 2 with $L = 333$ nm, $D = 140$ nm, and different values of thickness t. The incident light is an x-polarized plane wave with $\boldsymbol{k}||\hat{\boldsymbol{e}}_z$. The curve with the highest extinction peak is for $t = 230$ nm and subsequent curves are for $t = 140$, 80, 60, 50, 40, 30, 25, 20, and 15 nm. The extinction peak shows redshift as the film thickness t is decreased.

Transmittance resonances were found in theoretical studies of gold films perforated by a periodic array of square-shaped holes.[24] The resonances were shown to be redshifted as the film thickness is decreased and were seen to be closely linked to the excitation of SP's.[24] Furthermore, in the seminal work by Hessel and Oliner[30] it was shown that surface waves can cause anomalies in an optical grating system. Inspired by these, we investigate if a simple SP model can be used to explain the extinction peaks in Fig. 4.

The dispersion relation $\boldsymbol{k}_{\rm sp}(\lambda)$ of the SP $\boldsymbol{k}$ vector is known for continuous metal films (see Appendix A for details). We will use this dispersion relation to obtain estimations for the wavelengths for which incident light can excite SP's in the perforated gold film system. The validity of these predictions depends on how much the holes perturb the SP dispersion relation of a continuous film. Assume that a metal film is periodic in the x and y directions with periodicities L_x and L_y, respectively, and that the metal film is illuminated by a plane wave from a direction given by $\boldsymbol{k} = (k_x, k_y, k_z)$. The allowed $\boldsymbol{k}$ vectors in the x-y plane are then constrained to a discrete set given by

$$\boldsymbol{k}_{n_x,n_y} = \left(k_x + \frac{2\pi n_x}{L_x}\right)\hat{\boldsymbol{e}}_x + \left(k_y + \frac{2\pi n_y}{L_y}\right)\hat{\boldsymbol{e}}_y, \tag{56}$$

where n_x and n_y are integers. The real part of the SP $\boldsymbol{k}$ vector must equal one of the allowed $\boldsymbol{k}$ vectors in the x-y plane, i.e., one of $\boldsymbol{k}_{n_x,n_y}$. Because of this, SP's cannot be excited for any arbitrary (free-space) wavelength, but only for a discrete set of wavelengths, denoted by λ_{n_x,n_y}, for which the matching

$$\left|\mathrm{Re}\boldsymbol{k}_{\rm sp}\left(\lambda_{n_x,n_y}\right)\right| = \left|\boldsymbol{k}_{n_x,n_y}\right| \tag{57}$$

holds. For the systems we consider in this work, $L_x = L_y = L$, $\boldsymbol{k}||\hat{\boldsymbol{e}}_z$ and Eq. (57) can be simplified to

$$\left|\mathrm{Re}\boldsymbol{k}_{\rm sp}\left(\lambda_{n_x,n_y}\right)\right| = \frac{2\pi}{L}\sqrt{n_x^2 + n_y^2}. \tag{58}$$

We call this the simple SP model when we use the SP dispersion of a continuous film to give estimations for the wavelength for which SP's are expected to be excited in a perforated system.

The SP's in a continuous film belong to one of two branches, i.e., either the short- or the long-wavelength branch (see Appendix A for details). In the following, we use $\lambda^{\rm short}_{(n_x,n_y)}$ and $\lambda^{\rm long}_{(n_x,n_y)}$, where $\lambda^{\rm long}_{(n_x,n_y)} \geqslant \lambda^{\rm short}_{(n_x,n_y)}$ denote the predicted wavelengths of the long- and the short-wavelength branches, respectively. In the limit $t \to \infty$, an SP is localized to either the SiO_2/Au or the H_2O/Au interface. In this limit, $\lambda^{\rm short} \to \lambda^{\rm H_2O/Au}$, where $\lambda^{\rm H_2O/Au}$ is the wavelength for which an SP is allowed at an H_2O/Au interface. Similarly, when $t \to \infty$, $\lambda^{\rm long} \to \lambda^{\rm SiO_2/Au}$, where $\lambda^{\rm SiO_2/Au}$ is the wavelength for which an SP is allowed at an SiO_2/Au interface. To simplify the discussion, we call the SP that can be excited at $\lambda^{\rm short}_{(n_x,n_y)}$ the (n_x,n_y) SP of the short-wavelength branch. Similarly, we call the SP that can be excited at $\lambda^{\rm long}_{(n_x,n_y)}$ the (n_x,n_y) SP of the long-wavelength branch. Note that, as seen from Eq. (58), the $(\pm n_x,n_y)$, $(\pm n_x,-n_y)$, $(\pm n_y,n_x)$, and $(\pm n_y,-n_x)$ SP's of a given branch are degenerate and propagate in different directions given by Eqs. (56)–(58).

TABLE I. Wavelengths $\lambda_{(1,0)}^{\text{long}}$ for which SP's in a periodically perforated gold film system could be excited according to the matching in Eq. (58). Here, the SP dispersion of a continuous film of gold of thickness t sandwiched between H_2O and SiO_2 is used. The period of the structure is $L_x = L_y = 333$ nm. The incident light is a plane wave with $\boldsymbol{k}||\hat{\boldsymbol{e}}_z$. Only the longest wavelength solution (a long-wavelength branch) is shown for each thickness. The extinction peak positions λ_{peak} extracted from Fig. 4 are also shown.

t (nm)	$\lambda_{(1,0)}^{\text{long}}$ (nm)	λ_{peak} (nm)
230	569	569
140	569	571
80	572	590
60	580	614
50	588	631
40	603	655
30	628	692
25	648	720
20	679	758
15	727	816

We show in Table I $\lambda_{(1,0)}^{\text{long}}$ and the extinction peak positions extracted from Fig. 4. The extracted extinction peak positions for the two thickest films of $t = 230$ and 140 nm are very close to the corresponding values of $\lambda_{(1,0)}^{\text{long}}$. This indicates that SP's might be the cause of the extinction peaks in thick films and that the peak positions can be estimated from the simple SP model. We vary now D to make sure that this good agreement for thick films is not caused by a lucky choice of D. The extinction spectra for $t = 230$ nm are shown in Fig. 5 for $D = 40, 65, 90,$ 140, and 170 nm. The extinction peak position does not move noticeably when D is changed, indicating that the extinction peaks for the thick films shown in Fig. 5 are not caused by localized resonances at the holes. We notice further from Fig. 5

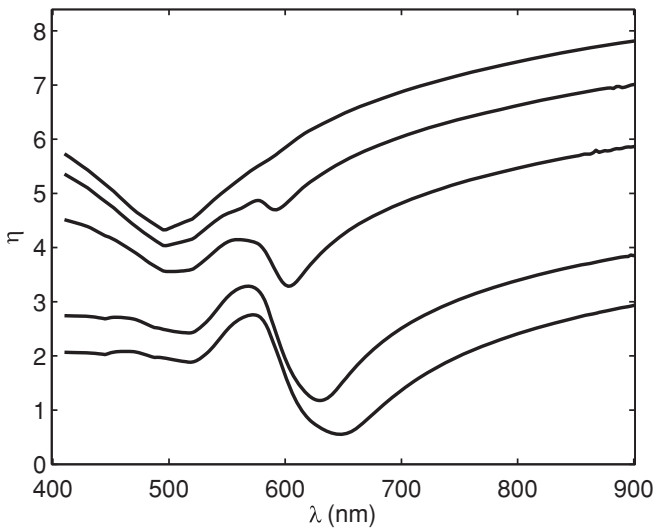

FIG. 5. Calculated extinction spectra for the system shown in Figs. 1 and 2 with $L = 333$ nm, $t = 230$ nm, and different values of D. The incident light is an x-polarized plane wave with $\boldsymbol{k}||\hat{\boldsymbol{e}}_z$. The top curve is for $D = 40$ nm and subsequent curves are for $D = 65$, 90, 140, and 170 nm.

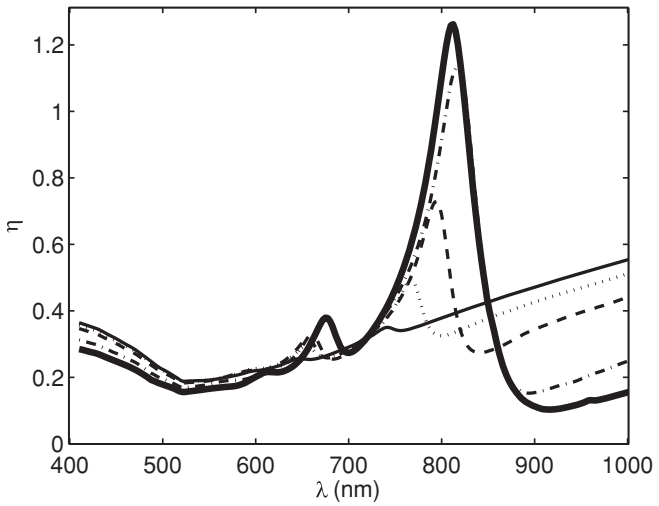

FIG. 6. Calculated extinction spectra for the system shown in Figs. 1 and 2 with $L = 333$ nm and $t = 15$ nm, and with $D = 170$ nm (thicker solid line), 140 nm (dashed-dotted line), 90 nm (dashed line), 65 nm (dotted line), and 40 nm (thinner solid line). The incident light is an x-polarized plane wave with $\boldsymbol{k}||\hat{\boldsymbol{e}}_z$.

that the peak weakens as D is decreased. For $D = 40$ nm, the peak is no longer visible. This is expected since normally incident light cannot couple to SP's in continuous films. It is the holes that enable the excitation of SP's. When the holes are made smaller, their ability to excite SP's is expected to be weakened.

When t decreases, both the extinction peak seen in Fig. 4 and $\lambda_{(1,0)}^{\text{long}}$ given in Table I show redshifts. However, the extinction peak in Fig. 4 shows a much larger redshift than the corresponding $\lambda_{(1,0)}^{\text{long}}$. For $t = 15$ nm, $\lambda_{(1,0)}^{\text{long}} = 727$ nm and the extinction peak is at $\lambda = 816$ nm. As explained above, $\lambda_{(1,0)}^{\text{long}}$ is obtained using the continuous film SP dispersion. This is the exact SP dispersion of the perforated film in the limit $D \to 0$. It is, therefore, of interest to investigate how the extinction peak position for thin films depends on D. The effect of varying D is shown in Fig. 6 for $t = 15$ nm. The peak moves toward $\lambda_{(1,0)}^{\text{long}}$ as D decreases. For the smallest considered diameter of $D = 40$ nm, the peak is at $\lambda = 741$ nm, which is only 14 nm away from $\lambda_{(1,0)}^{\text{long}} = 727$ nm. This indicates that SP's can cause extinction peaks in thin perforated films.

To explore further how SP's cause extinction peaks, we now vary the parameters that affect the wavelengths of extinction peaks in our perforated gold film systems and compare the results with the wavelengths for which the excitation of SP's is predicted based on our simple continuous film SP model. These parameters are L, t, and the refractive indices of the dielectric materials surrounding the metal plate.

We start by varying L for a thick plate. The extinction spectra for $t = 230$ nm and $D = 140$ nm are shown in Fig. 7 for $L = 333, 360, 400,$ and 450 nm. The number of peaks and the peak positions have strong dependencies on L. For $L = 333$ nm shown in Fig. 7(a), one peak exists. The same is true for $L = 360$ nm in Fig. 7(b). For $L = 400$ nm in Fig. 7(c) two peaks exist, while for $L = 450$ nm in Fig. 7(d) three peaks exist. In Table II, the wavelengths, for which SP's can be excited in an unperforated film, are shown for

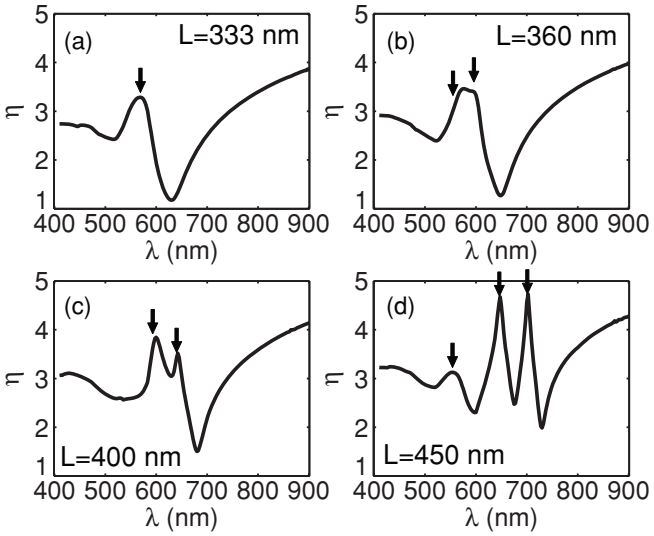

FIG. 7. Calculated extinction spectra for the system shown in Figs. 1 and 2 with $t = 230$ nm and $D = 140$ nm, and with $L = 333$ nm (a), 360 nm (b), 400 nm (c), and 450 nm (d). The incident light is an x-polarized plane wave with $\boldsymbol{k}||\hat{\boldsymbol{e}}_z$. The arrows in the figures indicate the predicted positions of the wavelengths, given in Table II, by the simple SP model, at which the SP's could be excited.

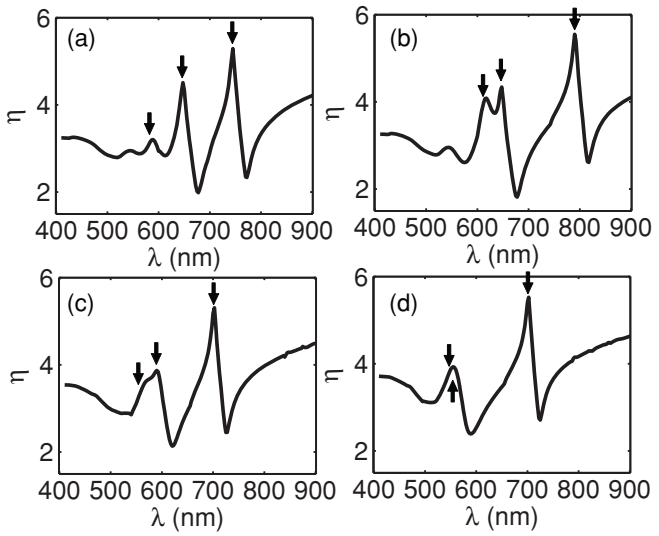

FIG. 8. Calculated extinction spectra for the system shown in Figs. 1 and 2 with $L = 450$ nm, $t = 230$ nm, and $D = 140$ nm. The incident light is an x-polarized plane wave with $\boldsymbol{k}||\hat{\boldsymbol{e}}_z$. The case in which the refractive index of the SiO_2 is artificially increased to $n = 1.55$ is shown in (a), while (b) shows the case of the increase to $n = 1.65$. The case in which the refractive index of the H_2O is artificially decreased to $n = 1.2$ is shown in (c), while (d) shows the case of the decrease to $n = 1.1$. The arrows in the figures indicate the predicted positions of the wavelengths, by the simple SP model, at which the SP's could be excited.

the different L. These wavelengths are indicated by arrows in Fig. 7. When these wavelengths are compared to the positions of the extinction peaks of our perforated gold film system for the varying L shown in Fig. 7, a good matching is found. For $L = 333$ nm, the (1,0) SP of the long-wavelength branch is expected to be excited at $\lambda^{\text{long}}_{(1,0)} = 569$ nm. The extinction spectrum for $L = 333$ nm in Fig. 7(a) shows a peak close to this wavelength. For $L = 360$ nm, the wavelengths, for which the excitation of SP's is expected, are $\lambda^{\text{short}}_{(1,0)} = 555$ nm and $\lambda^{\text{long}}_{(1,0)} = 596$ nm. The extinction spectrum for $L = 360$ nm in Fig. 7(b) shows a broadened peak at this wavelength range. We believe that this broadened peak is caused by two close-lying peaks at the estimated wavelengths. For $L = 400$ nm, SP's are expected to be excited at $\lambda^{\text{short}}_{(1,0)} = 593$ nm and $\lambda^{\text{long}}_{(1,0)} = 640$ nm and the extinction spectrum in Fig. 7(c) shows peaks at wavelengths very close to these wavelengths. Finally, for $L = 450$ nm, the wavelengths, for which SP's are expected to be excited, are $\lambda^{\text{long}}_{(1,0)} = 701$ nm, $\lambda^{\text{short}}_{(1,0)} = 646$ nm, and $\lambda^{\text{long}}_{(1,1)} = 554$ nm. The extinction spectrum for $L = 450$ nm in Fig. 7(d) shows peaks at wavelengths close to these wavelengths.

TABLE II. Wavelengths $\lambda^{\text{long}}_{(1,0)}$, $\lambda^{\text{short}}_{(1,0)}$, and $\lambda^{\text{long}}_{(1,1)}$ for which SP's in a periodically perforated gold film system could be excited according to the matching in Eq. (58). Here, again, the SP dispersion of a continuous film of gold of thickness $t = 230$ nm sandwiched between H_2O and SiO_2 is used. The period of the structure is $L_x = L_y = L$. The incident light is a plane wave with $\boldsymbol{k}||\hat{\boldsymbol{e}}_z$.

L (nm)	$\lambda^{\text{long}}_{(1,0)}$ (nm)	$\lambda^{\text{short}}_{(1,0)}$ (nm)	$\lambda^{\text{long}}_{(1,1)}$ (nm)
333	569		
360	596	555	
400	640	593	
450	701	646	554

The metal film of $t = 230$ nm studied above is so thick that the SP's in a continuous film are localized either to the left or to the right interface with a negligible coupling between the SP's localized at the two different interfaces. Thus, as discussed above, the short- (long-) wavelength branch corresponds to SP's at the H_2O/Au (SiO_2/Au) interface. It is then expected that the extinction peak position is more sensitive to a change in the refractive index of the dielectric closest to the interface where the SP is localized than to a change in the refractive index of the dielectric on the opposite side. To test this, we study the systems with artificially increased values of the refractive index of SiO_2 to 1.55 and 1.65 or artificially decreased values of the refractive index of H_2O to 1.1 and 1.2 for $L = 450$ nm. The extinction spectra are shown in Fig. 8 for these four cases together with arrows that show the wavelengths, given below, for which the simple SP model predicts possible excitation of SP's. When the refractive index of SiO_2 is increased, the wavelengths for which SP's are expected to be excited at the SiO_2/Au interface are $\lambda^{\text{long}}_{(1,1)} = 582$ nm and $\lambda^{\text{long}}_{(1,0)} = 744$ nm for $n = 1.55$, while for $n = 1.65$ they are $\lambda^{\text{long}}_{(1,1)} = 611$ nm and $\lambda^{\text{long}}_{(1,0)} = 790$ nm. The wavelengths for which SP's are expected to be excited at the H_2O/Au interface are $\lambda^{\text{short}}_{(1,0)} = 646$ nm for both cases. Both the extinction spectrum in Fig. 8(a) corresponding to an increase of the refractive index of SiO_2 to $n = 1.55$ and the spectrum in Fig. 8(b) corresponding to an increase to $n = 1.65$ show three peaks each. When these peak positions are compared to the corresponding estimated wavelengths above, a very good agreement is found. When the refractive index of H_2O is decreased, the wavelengths for which SP's are expected to

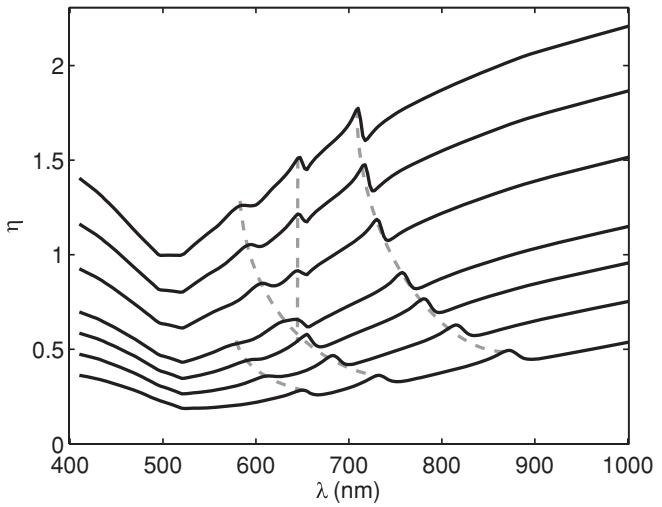

FIG. 9. Calculated extinction spectra for the system shown in Figs. 1 and 2 with $L = 450$ nm, $D = 65$ nm, and different values of t. The incident light is an x-polarized plane wave with $\boldsymbol{k}||\hat{\boldsymbol{e}}_z$. The top curve is for $t = 60$ nm and subsequent curves are for $t =$ 50, 40, 30, 25, 20, and 15 nm. The dashed lines are placed to guide the eyes.

be excited at the H_2O/Au interface are $\lambda^{\text{short}}_{(1,0)} = 589$ nm for $n = 1.2$ and $\lambda^{\text{short}}_{(1,0)} = 547$ nm for $n = 1.1$. The predictions for the SP's at the SiO_2/Au interface are $\lambda^{\text{long}}_{(1,1)} = 554$ nm and $\lambda^{\text{long}}_{(1,0)} = 701$ nm for both cases. Both the extinction spectrum in Fig. 8(c) corresponding to a decrease of the refractive index of H_2O to $n = 1.2$ and the spectrum in Fig. 8(d) corresponding to a decrease to $n = 1.1$ show a peak close to $\lambda^{\text{long}}_{(1,0)} = 701$ nm. For the case of $n = 1.2$ in Fig. 8(c) there is also a broad peak at $\lambda \approx 550 - 600$ nm. The position and the broadening of this peak agrees well with the estimated positions of $\lambda^{\text{short}}_{(1,0)} = 589$ nm and $\lambda^{\text{long}}_{(1,1)} = 554$ nm. For $n = 1.1$ in Fig. 8(d), there is, in addition to the peak close to $\lambda^{\text{long}}_{(1,0)} = 701$ nm, a peak at $\lambda \approx 550$ nm. This position agrees with the expected positions of the two close-lying SP's at $\lambda^{\text{short}}_{(1,0)} = 549$ nm and $\lambda^{\text{long}}_{(1,1)} = 554$ nm.

As the final step in the study of the parameters that affect the SP excitations and thus the extinction spectra, we consider a system exhibiting extinction peaks of both the long- and the short-wavelength SP branch in a thick film and study the effect of decreasing thickness t. For this, we choose the system of $L = 450$ nm and $D = 65$ nm. The extinction spectra are shown in Fig. 9 for $t = 15$–60 nm. The positions of two of the extinction peaks, one at $\lambda \approx 710$ nm and the other at $\lambda \approx 580$ nm, for $t = 60$ nm agree well with the estimated values of $\lambda^{\text{long}}_{(1,0)} = 706$ nm and $\lambda^{\text{long}}_{(1,1)} = 566$ nm given in Table III. As t decreases, these two extinction peaks show larger redshifts than the corresponding values of $\lambda^{\text{long}}_{(1,0)}$ and $\lambda^{\text{long}}_{(1,1)}$, but the deviations are less than 30 nm for all considered values of t. The peaks located close to $\lambda = 610$ nm at $t = 20$ nm and close to $\lambda = 650$ nm at $t = 15$ nm agree reasonably well with the estimated values of $\lambda^{\text{long}}_{(2,0)} = 587$ nm for $t = 20$ nm and $\lambda^{\text{long}}_{(2,0)} = 622$ nm for $t = 15$ nm for the (2,0) SP's of the long-wavelength branch. The peak at $\lambda \approx 645$ nm

TABLE III. Wavelengths $\lambda^{\text{long}}_{(1,0)}$, $\lambda^{\text{short}}_{(1,0)}$, and $\lambda^{\text{long}}_{(1,1)}$ for which SP's in a periodically perforated gold film system could be excited according to the matching in Eq. (58). The SP dispersion of a continuous film of gold of thickness t sandwiched between H_2O and SiO_2 is used here. The period of the structure is $L_x = L_y = 450$ nm. The incident light is a plane wave with $\boldsymbol{k}||\hat{\boldsymbol{e}}_z$.

t (nm)	$\lambda^{\text{long}}_{(1,0)}$ (nm)	$\lambda^{\text{short}}_{(1,0)}$ (nm)	$\lambda^{\text{long}}_{(1,1)}$ (nm)
230	701	646	554
140	701	646	554
80	702	646	557
60	706	645	566
50	711	644	576
40	726		591
30	746		615
25	767		635
20	799		665
15	851		712

for $t = 60$ nm is close to $\lambda^{\text{short}}_{(1,0)} = 645$ nm. This peak shows a completely different behavior compared to the peaks caused by the long-wavelength SP's discussed above. This peak does not move considerably, but dampens as t decreases and has disappeared when $t \leqslant 25$ nm. The reason for the negligibly small shift in the peak position with decreasing t is that the peak is caused by the excitation of the (1,0) SP mode of the short-wavelength branch, which is strongly localized at the Au/H_2O interface. Thus, the influence on the peak position by the dielectric SiO_2 on the other side of the gold film is negligible before the peak disappears. The disappearance of the peak can be understood with the help of our simple SP model as follows. As t decreases, if the dielectrics on the left and right sides of the film are not equal, the SP mode of the short-wavelength branch changes character at a certain critical thickness (see Appendix A and Ref. 50). For t smaller than this critical thickness, the SP field grows exponentially away from the film in one of the dielectrics.[50] Such a growing mode cannot physically exist and thus cannot be excited by incident light. From Table III, it is seen that $\lambda^{\text{short}}_{(1,0)}$ exhibits a blueshift only by 2 nm when t is decreased from 230 to 50 nm. At $t \leqslant 40$ nm, the (1,0) SP of the short-wavelength branch does not exist or has changed its characteristics to a growing mode. It is therefore expected that the extinction peak disappears at $t \leqslant 40$ nm since the SP causing the peak does not exist or cannot be excited.

Finally, we complete this subsection by presenting the results of calculations for the reflectance spectra, together with the extinction spectra, for a thick and a thin gold film system. First, we present the results of the calculations for a thick gold film system with $L = 450$ nm, $D = 65$ nm, and $t = 230$ nm (cf. Figs. 1 and 2). Figure 10 shows the extinction spectrum and the reflectance spectra of the system for x-polarized light incident normally from the SiO_2 side and from the H_2O side. The extinction spectrum shows two peaks at $\lambda = 701$ and 646 nm and two dips at $\lambda = 707$ and 654 nm. These characteristic wavelengths again coincide with or are very close to the values of $\lambda^{\text{long}}_{(1,0)} = 701$ nm and $\lambda^{\text{short}}_{(1,0)} = 646$ nm given in Tables II and III. We now discuss the

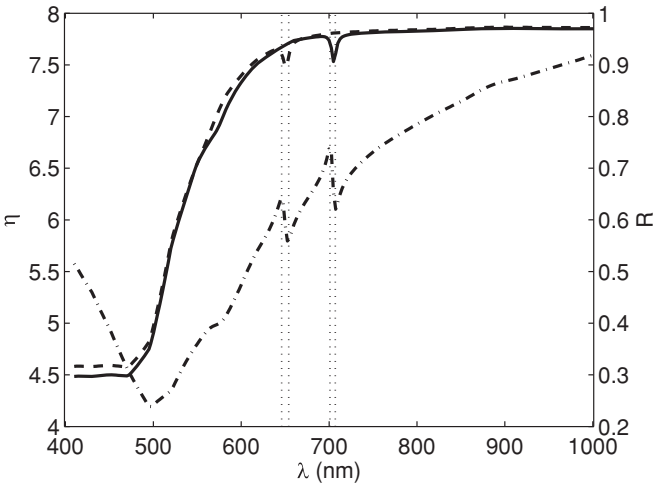

FIG. 10. Reflectance of the system shown in Figs. 1 and 2 with $L = 450$ nm, $D = 65$ nm, and $t = 230$ nm for light incident from the left (solid line) and from the right (dashed line), and extinction (dashed-dotted line) of the system. The vertical lines are placed at $\lambda = 646$, 654, 701, and 707 nm to guide the eyes. The incident light is an x-polarized plane wave with $\boldsymbol{k}||\hat{\boldsymbol{e}}_z$.

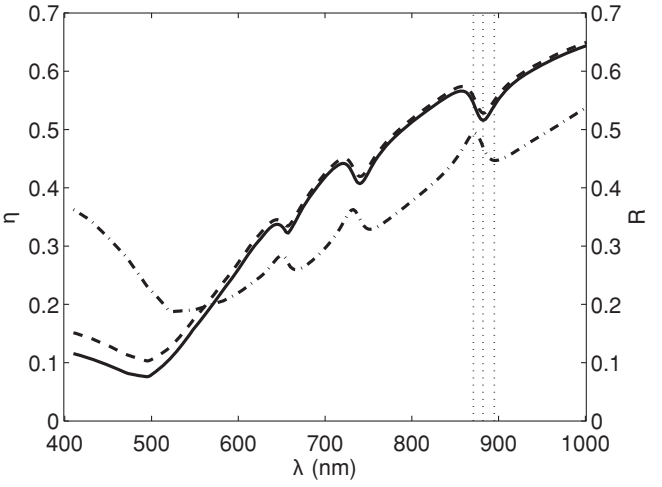

FIG. 11. Reflectance of the system shown in Figs. 1 and 2 with $L = 450$ nm, $D = 65$ nm, and $t = 15$ nm for light incident from the left (solid line) and from the right (dashed line), and extinction (dashed-dotted line) of the system. The vertical lines are placed at $\lambda = 871$, 882, and 895 nm to guide the eyes. The incident light is an x-polarized plane wave with $\boldsymbol{k}||\hat{\boldsymbol{e}}_z$.

reflectance spectra of the system. Here, we note that when we consider the reflectance, in contrast to the extinction, we need to discriminate from which side the light is incident. When the light is incident from the SiO_2 side, there is a dip in the reflectance at $\lambda = 705$ nm. This is close to $\lambda^{\text{long}}_{(1,0)} = 701$ nm, where an SP is expected to be excited at the SiO_2/Au interface. When the light is incident from the H_2O side, there is a dip in the reflectance at $\lambda = 651$ nm. This is close to $\lambda^{\text{short}}_{(1,0)} = 646$ nm, where an SP is expected to be excited at the H_2O/Au interface. Here, it is interesting to note that the reflectance shows one dip between each pair of extinction peak and dip for light incident from the left or from the right.

The second system considered here is a thin gold film with $t = 15$ nm, $L = 450$ nm, and $D = 65$ nm. When the film thickness is decreased, two factors need to be taken into consideration. First, the SP's on both interfaces of the thin film start to couple and a significant field intensity of the SP's could be found inside the film. Second, the transmission is not necessarily dominated by passing through the holes any longer. For instance, in a continuous (unperforated) gold film of $t = 15$ nm sandwiched between SiO_2 and H_2O, 34% of the incident intensity of normally incident light at $\lambda = 871$ nm can be transmitted. Figure 11 shows the reflectance spectra of the perforated gold film system of $t = 15$ nm with $L = 450$ nm and $D = 65$ nm for light incident from the left and from the right, as well as the extinction spectrum. The extinction spectrum shows a peak at $\lambda = 871$ nm and a dip at $\lambda = 895$ nm. We have identified this extinction peak, from Fig. 9, as being caused by the SP of the (1,0) long-wavelength branch. Between these two wavelengths, the reflectance shows a dip at $\lambda = 882$ nm both for light incident from the left and for light incident from the right. This is in contrast to the reflectance of the thicker film of $t = 230$ nm shown in Fig. 10, where the reflectance shows a dip only when the SP's are expected to be excited at the incidence side of the gold film. This is an indication that in the thinner film of $t = 15$ nm, the SP's can affect the reflectance regardless of which side the light is incident. The extinction spectrum shown in Fig. 11 exhibits peaks also at $\lambda = 732$ and 650 nm, with accompanying extinction dips at slightly longer wavelengths. These two extinction peaks have been identified, from Fig. 9, as being caused by the (1,1) and (2,0) SP's of the long-wavelength branch, respectively. It is also clearly seen again that the reflectance shows one dip between each pair of extinction peak and dip.

Thus, we have found that an extinction peak is accompanied by an extinction dip in both the thick (Fig. 10) and the thin (Fig. 11) film, and that a reflectance dip is located between the extinction peak and dip. This arrangement of an extinction peak, a reflectance dip, and an extinction dip seems to be a general property of the SP excitation.

B. Electromagnetic fields at SP resonances

In the above investigation, we concentrated on the excitation spectra. In the following, we will study the electromagnetic field distributions at the SP resonances to obtain a deeper understanding of the excitation spectra of the perforated gold film structures. We will consider the thick-film system studied in Fig. 10 and the thin-film system studied in Fig. 11. Figure 12 shows the electric-field distributions, $|E_z|$, $|E_x|$, and $|\boldsymbol{E}|^2$, of the system with $t = 230$ nm, $D = 65$ nm, and $L = 450$ nm, whose spectra were shown in Fig. 10. These field distributions are shown in the SiO_2/Au interface and a vertical cross section perpendicular to the interface for the x-polarized light incident normally from the SiO_2 side at wavelengths of $\lambda = 701$, 705, and 707 nm. At these wavelengths, only the zeroth-order diffracted modes are of a propagating kind in the SiO_2. These modes have no z component in the electric field. E_z in the near-field region on the SiO_2 side is thus caused by localized SP modes. This makes E_z well suited for the study of SP's. The strength distribution of $|E_z|$ in the SiO_2/Au interface shown in Figs. 12(a), 12(e), and 12(i) is dominated by a standing wave

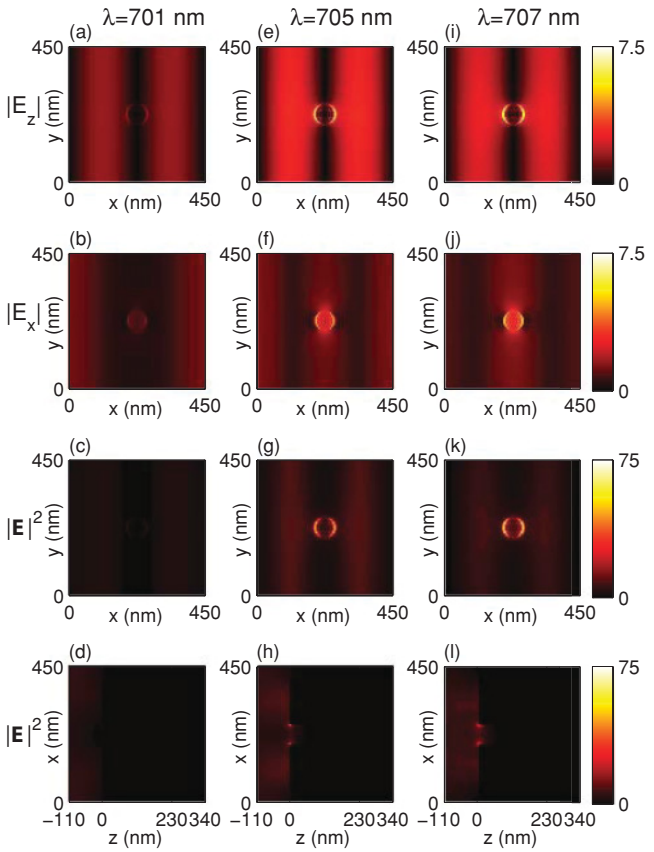

FIG. 12. (Color online) Calculated electric-field distributions for the system shown in Figs. 1 and 2 with $L = 450$ nm, $t = 230$ nm, and $D = 65$ nm at three different wavelengths. (a)–(d) are for $\lambda = 701$ nm, (e)–(h) are for $\lambda = 705$ nm, and (i)–(l) are for $\lambda = 707$ nm. $|E_z|$ in (a), (e), and (i), $|E_x|$ in (b), (f), and (j), and $|\boldsymbol{E}|^2$ in (c), (g), and (k) are the results at $z = 0$ nm on the SiO_2 side of the SiO_2/Au interface. $|\boldsymbol{E}|^2$ in (d), (h), and (l) shows the results at a vertical cross section that cuts through the $y = 225$ nm line and thus the middle of a hole. The gold film is placed at $t = 0$–230 nm. The incident light is a plane wave incident from the SiO_2 side with $\boldsymbol{E}^L || \hat{\boldsymbol{e}}_x$, $|\boldsymbol{E}^L| = 1$, and $\boldsymbol{k} || \hat{\boldsymbol{e}}_z$.

of the form $|\sin(2\pi x/L)|$ in the x direction with a noticeable deviation from this form in the vicinity of the hole. The decay of this standing wave away from the SiO_2/Au interface is of the form $e^{-\alpha|z|}$ with $\alpha \approx 5.0 \times 10^6$ m^{-1} on the SiO_2 side and $\alpha \approx 3.9 \times 10^7$ m^{-1} in the gold film. For comparison, we note that the decay constants of an SP at $\lambda = 701$ nm near the SiO_2/Au interface of a corresponding continuous film system are given by $\alpha = 4.98 \times 10^6$ m^{-1} on the SiO_2 side and $\alpha = 3.91 \times 10^7$ m^{-1} on the Au side. Thus, here we are observing the excitations of two counterpropagating SP's, the (1,0) and the (−1,0) modes, which cause the observed standing wave in Figs. 12(a), 12(e), and 12(i). It is also seen in Figs. 12(a), 12(e), and 12(i) that the excitation of the SP's is weakest, among these three considered wavelengths, at the extinction peak ($\lambda = 701$ nm) and strongest at the reflectance dip ($\lambda = 705$ nm). Figures 12(b), 12(f), and 12(j) show the calculated distribution of $|E_x|$ in the SiO_2/Au interface. Here, the excitation of the SP's is not seen as easily as in the plots for $|E_z|$, since $|E_x|$ has contributions from the incident and the reflected zeroth-order diffracted modes. It is, however, seen that the E_x field is strongly localized to the hole region at the extinction dip ($\lambda = 707$ nm) and the reflectance dip ($\lambda = 705$ nm). Figures 12(c), 12(g), and 12(k) and Figs. 12(d), 12(h), and 12(l) show the distributions of the total field strength $|\boldsymbol{E}|^2$ in the SiO_2/Au interface and in the vertical cross section cutting through the hole, respectively, at the three considered wavelengths. It is found that $|\boldsymbol{E}|^2$ has similar strengths in the hole region at the extinction dip and the reflectance dip. It is also found that at the extinction peak, the field is much weaker over the hole region than at the extinction dip and the reflectance dip. The penetration of $|\boldsymbol{E}|^2$ into the hole is also much smaller at the extinction peak than at the extinction dip and the reflectance dip.

When the wavelength is shifted from $\lambda = 701$ nm (at the extinction peak) to the shorter λ, the following is observed in the calculated electric-field distributions (not shown here). The SP's become less excited, $|\boldsymbol{E}|^2$ becomes stronger over the holes, and the penetration of the electric field into the holes becomes stronger. In comparison, when the wavelength is shifted from $\lambda = 707$ nm (at the extinction dip) to the longer λ, the following is observed in the calculated electric-field distributions (again not shown here). The SP's become less excited, $|\boldsymbol{E}|^2$ becomes weaker over the holes, and the penetration of the electric field into the holes also becomes weaker. These results are consistent with the observation of the extinction peak and dip, since the holes are the most effective transport path through a thick metal film. Furthermore, the estimations for the wavelength position of the extinction peak using the simple SP model are, as discussed above, expected to apply better for the perforated system when the field distribution in the hole regions is weaker. This is because at the extinction peak, $|\boldsymbol{E}|^2$ is weak in the vicinity of the holes [see Fig. 12(c)] and thus the field distribution of the SP in the periodically perforated metal film closely resembles the field distribution of the corresponding SP mode in the unperforated metal film.

The transmittance is negligible when the energy balance is considered at the SP resonance since $T < 10^{-6}$. Thus, the cause of the reflectance dip close to $\lambda = 705$ nm can be understood as a result of energy loss to Ohmic heat at the SP resonance. Since more energy is lost to Ohmic heat by the SP's, there is less energy available for the reflected light, and the reflectance dip occurs.

Figure 13 shows the $|E_z|$, $|E_x|$, and $|\boldsymbol{E}|^2$ field distributions of this system at the H_2O/Au interface when x-polarized light at wavelengths of $\lambda = 646$, 651, and 654 nm is incident from the SiO_2 side. The x and y dependencies of $|E_z|$ at the interface are also dominated here by a standing wave in the x direction. The decay of the standing wave away from the interface is again of the form $e^{-\alpha|z-t|}$. For $\lambda = 646$ nm, the decay constants are given by $\alpha \approx 5.2 \times 10^6$ m^{-1} and $\alpha \approx 3.8 \times 10^7$ m^{-1} in H_2O and the gold film, respectively. The decay constants of the SP mode at the H_2O/Au interface of the corresponding continuous film at $\lambda = 646$ nm are given by $\alpha = 5.21 \times 10^6$ m^{-1} on the H_2O side of the H_2O/Au interface and $\alpha = 3.74 \times 10^7$ m^{-1} on the Au side of the interface. This indicates that here we are observing the excitation of the (1,0) and (−1,0) SP's of the short-wavelength branch. As seen from Figs. 13(a), 13(e), and 13(i), the SP's are excited stronger at

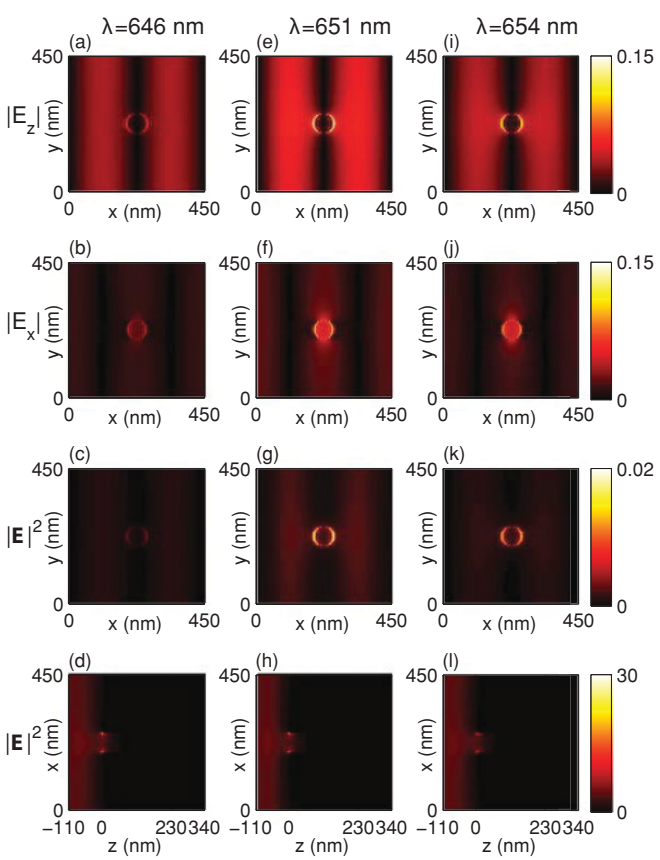

FIG. 13. (Color online) The same as in Fig. 12 but now for $\lambda =$ 646, 651, and 654 nm. Furthermore, (a)–(c), (e)–(g), and (i)–(k) show the results of the calculations at $z = 230$ nm on the H_2O side of the H_2O/Au interface.

$\lambda = 651$ nm than at the extinction peak or the extinction dip. A standing wave is seen also in $|E_x|$ in Figs. 13(b), 13(f), and 13(j). When Figs. 13(c), 13(g), and 13(k) are examined, it is found that $|\boldsymbol{E}|^2$ is much weaker in the vicinity of the holes at $\lambda = 646$ nm (extinction peak) than at $\lambda = 654$ nm (extinction dip) and $\lambda = 651$ nm. Figures 13(d), 13(h), and 13(l) show the distributions of the total field strength $|\boldsymbol{E}|^2$ in the vertical cross section cutting through the center of the hole in a unit cell. Here, we see that the field $|\boldsymbol{E}|^2$ has similar penetration strengths in the hole region at the three wavelengths of incident light, in strong contrast to the results shown in Figs 12(d), 12(h), and 12(l), where an SP very localized at the incident side SiO_2/Au interface is excited.

We now turn to study the electric-field distributions of the optically thin system with $L = 450$ nm, $D = 65$ nm, and $t = 15$ nm. Figure 14 shows the field distributions for an x-polarized incident light at $\lambda = 871$ nm, i.e., at one of the extinction peaks seen in Fig. 11. The field distributions $|E_z|$, $|E_x|$, and $|\boldsymbol{E}|^2$ at three x-y planes, i.e., the SiO_2/Au interface, central cross section, and H_2O/Au interface of the film, are shown in Fig. 14. Figures 14(a), 14(d), and 14(g) show $|E_z|$ at the three considered planes. It is seen that a standing wave is excited through the film (see also Fig. 15 for a line cut, at $y = 0$, that shows this more clearly). The standing wave has a low strength in the middle of the film. The decay constants

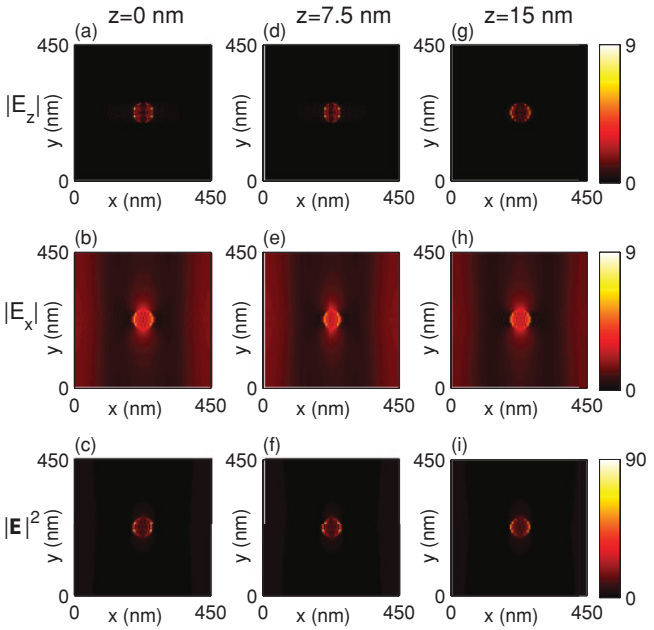

FIG. 14. (Color online) Calculated electric-field distributions for the system shown in Figs. 1 and 2 with $L = 450$ nm, $t = 15$ nm, and $D = 65$ nm at $\lambda = 871$ nm. (a)–(c) Results of the calculations at $z = 0$ nm on the Au side of the SiO_2/Au interface. (d)–(f) Results of the calculations at $z = 7.5$ nm. (g)–(i) Results of the calculations at $z = 15$ nm on the Au side of the H_2O/Au interface. $|E_z|$ is shown in (a), (d), and (g), $|E_x|$ in (b), (e), and (h), and $|\boldsymbol{E}|^2$ in (c), (f), and (i). The incident light is a plane wave incident from the SiO_2 side with $\boldsymbol{E}^L || \hat{\boldsymbol{e}}_x$, $|\boldsymbol{E}^L| = 1$, and $\boldsymbol{k} || \hat{\boldsymbol{e}}_z$.

of the standing wave into surrounding materials of the SiO_2 and the H_2O are found to be $\alpha = (9.1 \pm 0.5) \times 10^6$ m^{-1} and $\alpha = (10.1 \pm 0.5) \times 10^6$ m^{-1}, respectively. For comparison, we note that the SP of the long-wavelength branch in the corresponding continuous film at the wavelength of $\lambda^{\text{long}}_{(1,0)} =$ 851 nm has a decay constant $\alpha = 8.96 \times 10^6$ m^{-1} on the SiO_2 side of the SiO_2/Au interface and a decay constant $\alpha = 9.96 \times 10^6$ m^{-1} on the H_2O side of the H_2O/Au interface. Thus, we can attribute the standing wave to the excitation of the (1,0) and (−1,0) SP's of the long-wavelength branch in the thin film. Figures 14(b), 14(e), and 14(h) show $|E_x|$ at the three considered planes, where a standing-wave pattern is again seen. In comparison with the $|E_z|$ field distribution, the strength of $|E_x|$ does not show a strong z dependence inside the metal film. Furthermore, the standing-wave pattern of $|E_x|$ is out of phase to the standing-wave pattern of $|E_z|$. Figures 14(c), 14(f), and 14(i) show the distribution of $|\boldsymbol{E}|^2$. Here, a strong excitation of the electromagnetic wave localized in the hole region can be identified, in contrast to the distribution of $|\boldsymbol{E}|^2$ at the extinction peak in the thick film studied above. Thus, a significant deviation of the estimated wavelength $\lambda^{\text{long}}_{(1,0)} = 851$ nm for the excited SP's using the simple SP model from the actual value of $\lambda \sim 871$ nm is expected.

IV. CONCLUSIONS

In conclusion, we have formulated a scattering matrix method for the study of the response of a dissipative, metallic

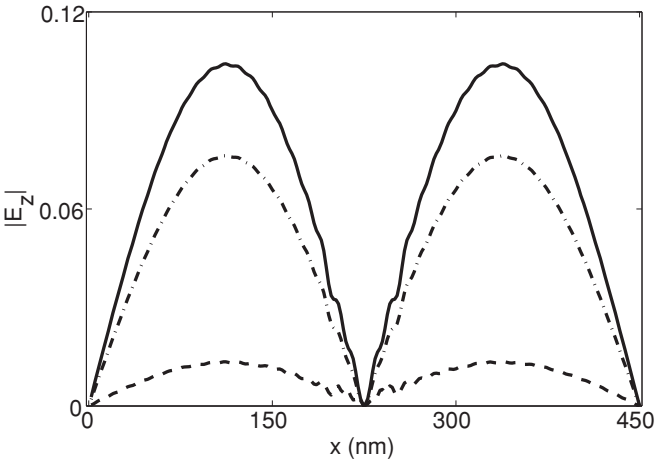

FIG. 15. Line plots of $|E_z|$ at $y = 0$ nm for the system shown in Figs. 1 and 2 with $L = 450$ nm, $t = 15$ nm, and $D = 65$ nm, at $\lambda = 871$ nm and $z = 0$ nm on the Au side of the SiO_2/Au interface (solid line), and $z = 7.5$ nm (dashed line) and $z = 15$ nm on the Au side of the H_2O/Au interface (dashed-dotted line). The incident light is a plane wave incident from the SiO_2 side with $\boldsymbol{E}^L || \hat{\boldsymbol{e}}_x$, $|\boldsymbol{E}^L| = 1$, and $\boldsymbol{k} || \hat{\boldsymbol{e}}_z$.

film system under the illumination of light. The method is general in the sense that it can be exploited to treat a metallic system patterned with an arbitrary subwavelength structure in arbitrary surrounding dielectric materials. The transmittance, reflectance, absorption, and extinction spectra of the system can be accurately calculated with the method. In addition, it is straightforward to employ the method to calculate the electromagnetic field distribution in the metallic system in both near-field and far-field regions. It is also straightforward to apply the method to a semiconductor system[51] as well as to a nondissipative dielectric system.

The formulated scattering matrix method has been applied to a system that consists of a gold film perforated by a periodic subwavelength hole array and two dielectric materials attached to the two sides of the film. The optical spectra of the system have been studied in great detail. In particular, the extinction spectra have been calculated for the gold film, with different hole diameters, hole periodicities, and film thicknesses, sandwiched between H_2O and SiO_2. In a thick film there exist extinction peaks at the wavelengths for which SP's are excited at either the SiO_2/Au or the H_2O/Au interface. When the thickness of the film is decreased, these peaks showed very different behaviors. The peaks caused by SP's at the SiO_2/Au interface in thick films shift toward longer wavelength with decreasing film thickness. The peaks caused by SP's at the H_2O/Au interface in thick films, however, do not shift noticeably. Instead, they are weakened as the film thickness is decreased and disappear eventually when the thickness of the film becomes smaller than a critical thickness. The extinction peak positions in thick films can be accurately predicted from the SP dispersion relation of a continuous gold film. For thin films with holes of small diameter, the peak positions can also be well estimated using the SP dispersion relation of a continuous gold film. We also find that for a thick film studied in this work, the positions of the extinction peaks do not move noticeably with a change in the diameter of holes. However, for thin films, when the diameter of the holes is increased, the peak positions show redshifts.

We have also calculated the electromagnetic field distributions in the perforated gold films at selected wavelengths. The electromagnetic field distributions in both the thick and the thin perforated films showed clearly the excitation of SP's at the extinction peaks, supporting our assignment of the transmission minima to the excitation of SP's in the systems. We have also found that in thick films with small holes, the electric-field strengths in the vicinity of the holes are weak at wavelengths for which extinction peaks occur. In contrast, it has been shown that for thin films at the extinction peak, a strong electric field can remain in the vicinity of the holes.

ACKNOWLEDGMENTS

This work was supported by the Swedish Research Council (VR), the Swedish Foundation for Strategic Research (SSF) through the Nanometer Structure Consortium at Lund University (nmC@LU), EU program AMON-RA (No. 214814), and E.ON AG as part of the E.ON International Research Initiative.

APPENDIX A: SURFACE-PLASMON DISPERSION IN CONTINUOUS FILMS

A summary of the SP dispersion in a continuous, nonmagnetic metal film is given here. The electric field of an SP in a system consisting of a continuous metal film of thickness t and permittivity $\tilde{\epsilon}_2$ and two surrounding materials of permittivities $\tilde{\epsilon}_1$ and $\tilde{\epsilon}_3$ is[50,52]

$$\boldsymbol{E}_{\rm sp}(\boldsymbol{x}) = \begin{cases} (E_{1,\rho}\hat{\boldsymbol{e}}_\rho + E_{1,z}\hat{\boldsymbol{e}}_z)e^{i(k_{\rm sp}\rho - k_{1,z}z)}, & z < 0 \\ (E_{3,\rho}\hat{\boldsymbol{e}}_\rho + E_{3,z}\hat{\boldsymbol{e}}_z)e^{i[k_{\rm sp}\rho + k_{3,z}(z-t)]}, & z > t \\ (E_{L,\rho}\hat{\boldsymbol{e}}_\rho + E_{L,z}\hat{\boldsymbol{e}}_z)e^{i(k_{\rm sp}\rho + k_{2,z}z)} & \\ +(E_{R,\rho}\hat{\boldsymbol{e}}_\rho + E_{R,z}\hat{\boldsymbol{e}}_z)e^{i[k_{\rm sp}\rho - k_{2,z}(z-t)]}, & 0 < z < t, \end{cases} \tag{A1}$$

where $\hat{\boldsymbol{e}}_\rho$ ($\hat{\boldsymbol{e}}_z$) is the unit vector parallel (perpendicular) to the film surface, $k_{\rm sp}$ is the in-plane k vector of the SP, and $\{k_{i,z}\}$ are the k vectors in the three material regions along the perpendicular z direction. To simplify notation, we call the interface between the dielectric of $\tilde{\epsilon}_1$ ($\tilde{\epsilon}_3$) and the metal film the interface 1/2 (2/3). The coordinate system is chosen so that $z = 0$ ($z = t$) corresponds to the interface 1/2 (2/3).

From the Maxwell equations, i.e., Eq. (4), $k_{\rm sp}(\lambda)$ must fulfill[29,52]

$$e^{2ik_{2,z}t}\left[\frac{\tilde{\epsilon}_1}{k_{1,z}} - \frac{\tilde{\epsilon}_2}{k_{2,z}}\right]\left[\frac{\tilde{\epsilon}_2}{k_{2,z}} - \frac{\tilde{\epsilon}_3}{k_{3,z}}\right] + \left[\frac{\tilde{\epsilon}_3}{k_{3,z}} + \frac{\tilde{\epsilon}_2}{k_{2,z}}\right]\left[\frac{\tilde{\epsilon}_1}{k_{1,z}} + \frac{\tilde{\epsilon}_2}{k_{2,z}}\right] = 0, \tag{A2}$$

where

$$k_{i,z}(\lambda) = \left[\frac{\tilde{\epsilon}_i(\lambda)}{\epsilon_0}\left(\frac{2\pi}{\lambda}\right)^2 - k_{\rm sp}(\lambda)^2\right]^{1/2}. \tag{A3}$$

We require that $\mathrm{Im}(k_{i,z}) \geqslant 0$ and $\mathrm{Im}(k_{\rm sp}) \geqslant 0$. In the case of $\mathrm{Im}(k_{\rm sp}) = 0$, we require also $\mathrm{Re}(k_{\rm sp}) \geqslant 0$. The surface mode in Eq. (A2) is therefore fixed to be, for our system, a physically relevant bound SP which we choose to decay and/or propagate

in the positive ρ direction. When $t \to \infty$, Eq. (A2) reduces to the more familiar single interface dispersion relation[29]

$$k_{sp}(\lambda) = \frac{2\pi}{\lambda}\left(\frac{\tilde{\epsilon}_j(\lambda)\tilde{\epsilon}_2(\lambda)}{\epsilon_0[\tilde{\epsilon}_j(\lambda)+\tilde{\epsilon}_2(\lambda)]}\right)^{1/2}, \tag{A4}$$

where $j = 1$ (3) when interface 1/2 (2/3) is considered.

The dispersion of $k_{sp}(\lambda)$ from Eq. (A2) in the interval of $[\lambda_{initial},\lambda_{final}]$ is calculated using the Newton-Raphson method as follows. We start our calculation of $k_{sp}(\lambda)$ from wavelength $\lambda_{initial}$ and a large value of t using a solution from Eq. (A4) corresponding to an SP on either the 1/2 or the 2/3 interface as an initial guess. Clearly, this gives two possible solution *branches*. After an actual solution to Eq. (A2) is found, t is decreased and λ is kept at the value of $\lambda_{initial}$. The solution to Eq. (A2) for the decreased value of t is then sought with the solution for the previously considered value of t as an initial guess. When the solution k_{sp} for $\lambda_{initial}$ and a considered value of t is found, t is kept fixed at the value and a sweep in λ is made. In this way, the dispersion $k_{sp}(\lambda)$ for the chosen branch and a considered value of t in the wavelength interval $[\lambda_{initial},\lambda_{final}]$ is constructed.

We consider now the specific case of a gold film sandwiched between SiO_2 and H_2O. This corresponds to the system shown in Figs. 1 and 2 in the limit of $D \to 0$. For a fixed $\mathrm{Re}(k_{sp})$ and large t, two wavelengths λ_1 and λ_2, with $\lambda_1 > \lambda_2$, which satisfy Eq. (A2), are obtained. SP's at λ_1 (λ_2) originate from the branch that corresponds to an SP at the SiO_2/Au (H_2O/Au) interface in the limit of $t \to \infty$. We therefore call the branch that stems from the SP at the SiO_2/Au (H_2O/Au) interface in the limit of $t \to \infty$ the long-wavelength (short-wavelength) branch. For the short-wavelength branch, a critical thickness $t_c(\lambda)$ exists. When $t < t_c(\lambda)$, no solution for a bound SP of the short-wavelength branch could be found at the wavelength λ. For example, for $615 < \lambda < 1000$ nm, $t = 40$ nm is already below the critical thickness. It is also found that the shift in $\mathrm{Re}[k_{sp}(\lambda)]$ with varying t for the short-wavelength branch is small. The reason why no solution could be found below the critical thickness is that the solution of the short-wavelength branch changes character at $t = t_c$. For $t < t_c$, the solution is no longer bound to the gold film.[50] Instead, it grows exponentially away from the gold film into one of the dielectrics.[50] We do not consider a surface mode of this kind as a physically relevant SP mode for our system.

It is found that the deviation between results for k_{sp} from the thin-film equation, Eq. (A2), and the single interface equation, Eq. (A4), is negligible for $t > 100$ nm. This means that for $t > 100$ nm, SP's on opposite surfaces should be almost completely decoupled. The calculated dispersion curves of $\mathrm{Re}[k_{sp}(\lambda)]$ for both the long-wavelength and the short-wavelength branches are shown in Fig. 16 for varying t. For the short-wavelength branch, only the curve for $t = 230$ nm is shown since the shift in this branch is small before the branch disappears. For a fixed $\mathrm{Re}(k_{sp})$, the long-wavelength branch shows a clear redshift as t is decreased.

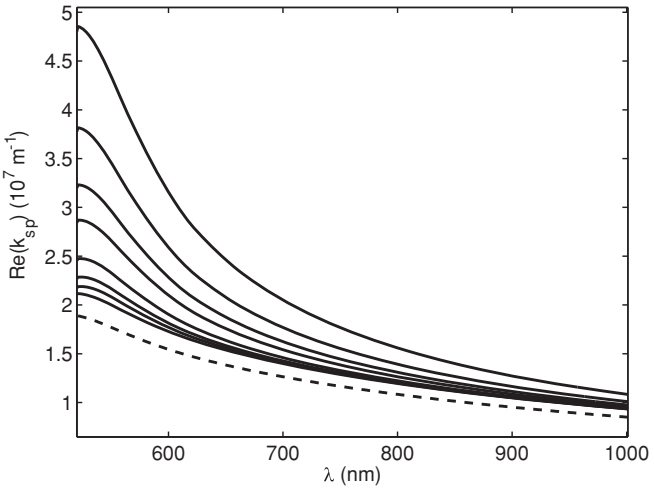

FIG. 16. $\mathrm{Re}[k_{sp}(\lambda)]$ for a continuous Au film of thickness t sandwiched between SiO_2 and H_2O. The solid curves are for the long-wavelength branch. In large thickness values of t, this branch converges to SP's at the SiO_2/Au interface with an infinitely thick gold film. The lowest solid curve is for $t = 230$ nm and subsequent curves are for $t = 60,50,40,30,25,20$, and 15 nm. The dashed curve is for the short-wavelength branch. Here, only the curve for $t = 230$ nm is shown. This is because no solutions exist for this branch when t becomes smaller than certain critical values and the shift in $\mathrm{Re}[k_{sp}(\lambda)]$ with varying t is small. In large thickness values of t, this branch converges to SP's at the H_2O/Au interface with an infinitely thick gold film.

APPENDIX B: FAST FOURIER FACTORIZATION

In the simulated periodic and nonmagnetic ($\tilde{\mu} = \mu_0$) system presented in Figs. 1 and 2, the media changes from gold to water at the rim of a hole. This makes $\tilde{\epsilon}_j(x,y)$ in Eqs. (7) and (8) discontinuous in the x-y plane in the $j = 1$ slice. In that case, the numerical convergence rate can be improved if the remarks made by Li in Ref. 53 on the Fourier factorization of products of pairwise discontinuous functions are taken into account. We take these remarks into account by the use of the fast Fourier factorization method in Ref. 48. This requires the introduction of the vector field $\boldsymbol{N}_j(x,y) = N_{j,x}(x,y)\hat{\boldsymbol{e}}_x + N_{j,y}(x,y)\hat{\boldsymbol{e}}_y$ that describes the discontinuity of $\tilde{\epsilon}_j(x,y)$ in slice j. The requirement on $\boldsymbol{N}_j$ is that it is normal to the discontinuity of $\tilde{\epsilon}_j$ and that $|\boldsymbol{N}_j| = 1$. Furthermore, $\boldsymbol{N}_j$ should be continuous along the discontinuity of $\tilde{\epsilon}_j$ and an extension of $\boldsymbol{N}_j$ should be made outside the discontinuity of $\tilde{\epsilon}_j$. The remarks made by Li[53] are taken into account by modifying $\boldsymbol{T}_1^j$ and $\boldsymbol{T}_2^j$ in Eqs. (7) and (8) slightly, giving[48]

$$\begin{aligned}
\boldsymbol{T}^j_{1,xx} &= \frac{1}{i\omega}\boldsymbol{D}_x\tilde{\boldsymbol{Q}}^{-1}_{j,\epsilon,zz}\boldsymbol{D}_y,\\
\boldsymbol{T}^j_{1,xy} &= -\frac{1}{i\omega}\boldsymbol{D}_x\tilde{\boldsymbol{Q}}^{-1}_{j,\epsilon,zz}\boldsymbol{D}_x + i\omega\mu_0\boldsymbol{1},\\
\boldsymbol{T}^j_{1,yx} &= -i\omega\mu_0\boldsymbol{1} + \frac{1}{i\omega}\boldsymbol{D}_y\tilde{\boldsymbol{Q}}^{-1}_{j,\epsilon,zz}\boldsymbol{D}_y,\\
\boldsymbol{T}^j_{1,yy} &= -\frac{1}{i\omega}\boldsymbol{D}_y\tilde{\boldsymbol{Q}}^{-1}_{j,\epsilon,zz}\boldsymbol{D}_x,\\
\boldsymbol{T}^j_{2,xx} &= -\frac{1}{i\omega\mu_0}\boldsymbol{D}_x\boldsymbol{D}_y - i\omega\tilde{\boldsymbol{Q}}_{j,\epsilon,xy},\\
\boldsymbol{T}^j_{2,xy} &= \frac{1}{i\omega\mu_0}\boldsymbol{D}_x\boldsymbol{D}_x - i\omega\tilde{\boldsymbol{Q}}_{j,\epsilon,yy},
\end{aligned} \tag{B1}$$

$$\boldsymbol{T}^{j}_{2,yx} = -\frac{1}{i\omega\mu_0}\boldsymbol{D}_y\boldsymbol{D}_y + i\omega\tilde{\boldsymbol{Q}}_{j,\epsilon,xx},$$
$$\boldsymbol{T}^{j}_{2,yy} = \frac{1}{i\omega\mu_0}\boldsymbol{D}_y\boldsymbol{D}_x + i\omega\tilde{\boldsymbol{Q}}_{j,\epsilon,xy},$$

where

$$\begin{aligned}\tilde{\boldsymbol{Q}}_{j,\epsilon,xx} &= \boldsymbol{A}_j - \left(\boldsymbol{A}_j - \boldsymbol{B}_j^{-1}\right)\tilde{\boldsymbol{N}}_{j,2x},\\ \tilde{\boldsymbol{Q}}_{j,\epsilon,yy} &= \boldsymbol{A}_j - \left(\boldsymbol{A}_j - \boldsymbol{B}_j^{-1}\right)\tilde{\boldsymbol{N}}_{j,2y},\\ \tilde{\boldsymbol{Q}}_{j,\epsilon,zz} &= \boldsymbol{A}_j,\\ \tilde{\boldsymbol{Q}}_{j,\epsilon,xy} &= -\left(\boldsymbol{A}_j - \boldsymbol{B}_j^{-1}\right)\tilde{\boldsymbol{N}}_{j,xy},\end{aligned} \tag{B2}$$

and

$$(\boldsymbol{D}_x)_{mn} = \langle\phi_m|\frac{\partial}{\partial x}|\phi_n\rangle,$$
$$(\boldsymbol{D}_y)_{mn} = \langle\phi_m|\frac{\partial}{\partial y}|\phi_n\rangle,$$

$$\begin{aligned}(\boldsymbol{A}_j)_{mn} &= \langle\phi_m|\tilde{\epsilon}_j(x,y)|\phi_n\rangle,\\ (\boldsymbol{B}_j)_{mn} &= \langle\phi_m|\tilde{\epsilon}_j(x,y)^{-1}|\phi_n\rangle,\\ (\tilde{\boldsymbol{N}}_{j,2x})_{mn} &= \langle\phi_m|N^2_{j,x}(x,y)|\phi_n\rangle,\\ (\tilde{\boldsymbol{N}}_{j,2y})_{mn} &= \langle\phi_m|N^2_{j,y}(x,y)|\phi_n\rangle,\\ (\tilde{\boldsymbol{N}}_{j,xy})_{mn} &= \langle\phi_m|N_{j,x}(x,y)N_{j,y}(x,y)|\phi_n\rangle.\end{aligned} \tag{B3}$$

For the system presented in Figs. 1 and 2, we chose, for $j = 1$ in the unit cell defined by $0 < x \leqslant L$ and $0 < y \leqslant L$, $N_{j,x}(x,y) = 1$ and $N_{j,y}(x,y) = 0$ when $x = L/2$ and $y = L/2$, and otherwise $N_{j,x}(x,y) = (x - L/2)/r$ and $N_{j,y}(x,y) = (y - L/2)/r$ with $r = \sqrt{(x - L/2)^2 + (y - L/2)^2}$. The values in the whole x-y plane are defined by $N_{j,x(y)}(x + mL, y + nL) = N_{j,x(y)}(x,y)$, with m and n being integers.

*Author to whom all correspondence should be addressed: hongqi.xu@ftf.lth.se

[1] T. W. Ebbesen, H. J. Lezec, H. F. Ghaemi, T. Thio, and P. A. Wolff, Nature (London) **391**, 667 (1998).
[2] C. Genet and T. Ebbesen, Nature (London) **445**, 39 (2007).
[3] H. F. Ghaemi, T. Thio, D. E. Grupp, T. W. Ebbesen, and H. J. Lezec, Phys. Rev. B **58**, 6779 (1998).
[4] A. Krishnan, T. Thio, T. J. Kim, H. J. Lezec, T. W. Ebbesen, P. A. Wolff, J. Pendry, L. Martin-Moreno, and F. J. Garcia-Vidal, Opt. Commun. **200**, 1 (2001).
[5] U. Schröter and D. Heitmann, Phys. Rev. B **58**, 15419 (1998).
[6] S.-H. Chang, S. K. Gray, and G. C. Schatz, Opt. Express **13**, 3150 (2005).
[7] E. Popov, M. Nevière, S. Enoch, and R. Reinisch, Phys. Rev. B **62**, 16100 (2000).
[8] Z. Ruan and M. Qiu, Phys. Rev. Lett. **96**, 233901 (2006).
[9] J. A. Porto, F. J. García-Vidal, and J. B. Pendry, Phys. Rev. Lett. **83**, 2845 (1999).
[10] L. Salomon, F. Grillot, A. V. Zayats, and F. de Fornel, Phys. Rev. Lett. **86**, 1110 (2001).
[11] J. R. DiMaio and J. Ballato, Opt. Express **14**, 2380 (2006).
[12] R. Gordon, A. G. Brolo, A. McKinnon, A. Rajora, B. Leathem, and K. L. Kavanagh, Phys. Rev. Lett. **92**, 037401 (2004).
[13] K. L. van der Molen, F. B. Segerink, N. F. van Hulst, and L. Kuipers, Appl. Phys. Lett. **85**, 4316 (2004).
[14] K. J. Klein Koerkamp, S. Enoch, F. B. Segerink, N. F. van Hulst, and L. Kuipers, Phys. Rev. Lett. **92**, 183901 (2004).
[15] K. L. van der Molen, K. J. Klein Koerkamp, S. Enoch, F. B. Segerink, N. F. van Hulst, and L. Kuipers, Phys. Rev. B **72**, 045421 (2005).
[16] P. Lalanne, J. C. Rodier, and J. P. Hugonin, J. Opt. A **7**, 422 (2005).
[17] F. Marquier, J.-J. Greffet, S. Collin, F. Pardo, and J. L. Pelouard, Opt. Express **13**, 70 (2005).
[18] L. Martín-Moreno, F. J. García-Vidal, H. J. Lezec, K. M. Pellerin, T. Thio, J. B. Pendry, and T. W. Ebbesen, Phys. Rev. Lett. **86**, 1114 (2001).
[19] Q. Cao and P. Lalanne, Phys. Rev. Lett. **88**, 057403 (2002).
[20] S. G. Rodrigo, F. J. García-Vidal, and L. Martín-Moreno, Phys. Rev. B **77**, 075401 (2008).
[21] P. Lalanne, C. Sauvan, J. P. Hugonin, J. C. Rodier, and P. Chavel, Phys. Rev. B **68**, 125404 (2003).
[22] J.-Q. Li, W.-Q. Yang, Y.-T. Zhang, Q.-J. Wang, C.-P. Huang, and Y.-Y. Zhu, J. Appl. Phys. **101**, 073505 (2007).
[23] J.-Y. Li, Y.-L. Hua, J.-X. Fu, and Z.-Y. Li, J. Appl. Phys. **107**, 073101 (2010).
[24] S. G. Rodrigo, L. Martín-Moreno, A. Yu. Nikitin, A. V. Kats, I. S. Spevak, and F. J. García-Vidal, Opt. Lett. **34**, 4 (2009).
[25] D. Z. Lin, C. K. Chang, Y. C. Chen, D. L. Yang, M. W. Lin, J. T. Yeh, J. M. Liu, C. H. Kuan, C. S. Yeh, and C. K. Lee, Opt. Express **14**, 3503 (2006).
[26] S. Kim, H. Kim, Y. Lim, and B. Lee, Appl. Phys. Lett. **90**, 051113 (2007).
[27] S. Kim, Y. Lim, H. Kim, J. Park, and B. Lee, Appl. Phys. Lett. **92**, 013103 (2008).
[28] Y. Liu, H. Shi, C. Wang, C. Du, and X. Luo, Opt. Express **16**, 4487 (2008).
[29] H. Raether, *Surface Plasmons on Smooth and Rough Surfaces and on Gratings* (Springer-Verlag, Berlin, 1988).
[30] A. Hessel and A. A. Oliner, Appl. Opt. **4**, 1275 (1965).
[31] K. Okamoto, I. Niki, A. Shvartser, Y. Narukawa, T. Mukai, and A. Scherer, Nature Mater. **3**, 601 (2004).
[32] N. Yu, J. Fan, Q. J. Wang, C. Pflügl, L. Diehl, T. Edamura, M. Yamanishi, H. Kan, and F. Capasso, Nature Phot. **2**, 564 (2008).
[33] J. Yao, A.-P. Le, S. K. Gray, J. S. Moore, J. A. Rogers, and R. G. Nuzzo, Adv. Mater. **22**, 1102 (2010).
[34] A. B. Dahlin, J. O. Tegenfeldt, and F. Höök, Anal. Chem. **78**, 4416 (2006).
[35] H. Q. Xu, Phys. Rev. B **50**, 8469 (1994).
[36] H. Q. Xu, Phys. Rev. B **52**, 5803 (1995).
[37] D. Csontos and H. Q. Xu, J. Phys. Condens. Matter **14**, 12513 (2002).
[38] L. Zhang, P. Brusheim, and H. Q. Xu, Phys. Rev. B **72**, 045347 (2005).

[39]L. Zhang, F. Zhai, and H. Q. Xu, Phys. Rev. B **74**, 195332 (2006).
[40]P. Brusheim and H. Q. Xu, Phys. Rev. B **74**, 205307 (2006).
[41]P. Brusheim, D. Csontos, U. Zülicke, and H. Q. Xu, Phys. Rev. B **78**, 085301 (2008).
[42]P. B. Johnson and R. W. Christy, Phys. Rev. B **6**, 4370 (1972).
[43]*CRC Handbook of Chemistry and Physics*, 82nd ed., edited by D. Lide (CRC, Cleveland, OH, 2001).
[44]H. R. Philipp, in *Handbook of Optical Constants of Solids*, edited by E. D. Palik (Academic, Orlando, FL, 1985), p. 749.
[45]Z.-Y. Li and L.-L. Lin, Phys. Rev. E **67**, 046607 (2003).
[46]L. Li, J. Mod. Opt. **40**, 553 (1993).
[47]D. Yuk Kei Ko and J. C. Inkson, Phys. Rev. B **38**, 9945 (1988).
[48]E. Popov and M. Nevière, J. Opt. Soc. Am. A **18**, 2886 (2001).
[49]M. Iwanaga, A. S. Vengurlekar, T. Hatano, and T. Ishihara, Am. J. Phys. **75**, 899 (2007).
[50]J. J. Burke, G. I. Stegeman, and T. Tamir, Phys. Rev. B **33**, 5186 (1986).
[51]N. Anttu and H. Q. Xu, J. Nanosci. Nanotechnol. **10**, 7183 (2010).
[52]C. A. Ward, K. Bhasin, R. J. Bell, R. W. Alexander, and I. Tyler, J. Chem. Phys. **62**, 1674 (1975).
[53]L. Li, J. Opt. Soc. Am. A **13**, 1870 (1996).